catalysts

MDPI

Review

Ambient Air Purification by Nanotechnologies: From Theory to Application

Jun-ji Cao [1,2,3,*], Yu Huang [1,2,3] and Qian Zhang [1,2]

[1] State Key Laboratory of Loess and Quaternary Geology (SKLLQG), Institute of Earth Environment, Chinese Academy of Sciences, Xi'an 710061, China; huangyu@ieecas.cn (Y.H.); zhangqian@ieecas.cn (Q.Z.)
[2] Key Laboratory of Aerosol Chemistry & Physics, Institute of Earth Environment, Chinese Academy of Sciences, Xi'an 710061, China
[3] Center of Excellence in Quaternary Science and Global Change, Chinese Academy of Sciences, Xi'an 710061, China
* Correspondence: cao@loess.llqg.ac.cn

Abstract: Air pollution has been a recurring problem in northern Chinese cities, and high concentrations of $PM_{2.5}$ in winter have been a particular cause for concern. Secondary aerosols converted from precursor gases (i.e., nitrogen oxides and volatile organic compounds) evidently account for a large fraction of the $PM_{2.5}$. Conventional control methods, such as dust removal, desulfurization, and denitrification, help reduce emissions from stationary combustion sources, but these measures have not led to decreases in haze events. Recent advances in nanomaterials and nanotechnology provide new opportunities for removing fine particles and gaseous pollutants from ambient air and reducing the impacts on human health. This review begins with overviews of air pollution and traditional abatement technologies, and then advances in ambient air purification by nanotechnologies, including filtration, adsorption, photocatalysis, and ambient-temperature catalysis are presented—from fundamental principles to applications. Current state-of-the-art developments in the use of nanomaterials for particle removal, gas adsorption, and catalysis are summarized, and practical applications of catalysis-based techniques for air purification by nanomaterials in indoor, semi-enclosed, and open spaces are highlighted. Finally, we propose future directions for the development of novel disinfectant nanomaterials and the construction of advanced air purification devices.

Keywords: nanotechnologies; air purification; photocatalysis; ambient-temperature catalysis

Citation: Cao, J-j.; Huang, Y.; Zhang, Q. Ambient Air Purification by Nanotechnologies: From Theory to Application. *Catalysts* **2021**, *11*, 1276. https://doi.org/10.3390/catal11111276

Academic Editor: María Victoria López Ramón

Received: 29 September 2021
Accepted: 18 October 2021
Published: 22 October 2021

Publisher's Note: MDPI stays neutral with regard to jurisdictional claims in published maps and institutional affiliations.

1. Introduction

China is facing daunting challenges in local and regional air quality due to its continued economic growth and industrialization. During the winters of 2013 and 2014, many of the cities in northern and eastern China (~15%) suffered from severe haze caused by particulate matter (PM) <2.5 μm in aerodynamic diameter ($PM_{2.5}$) [1]. High levels of $PM_{2.5}$ in the range of 500—800 μg/m^3 were recorded in one pollution episode in Beijing, and that resulted in strong impairments of visibility (<100 m) [2]. Other impacts of $PM_{2.5}$ pollution include adverse health effects, especially increased incidences of cardiorespiratory disease, as revealed in numerous toxicological studies [2]. In China, 1.1 million deaths in 2015 were ascribed to long-term exposure to high levels of $PM_{2.5}$ [3]. Thus, the following questions concerning the problem should be addressed: (1) what is the composition of $PM_{2.5}$? (2) what are the causes of severe haze formation? and (3) how can haze formation be controlled? An et al. published a comprehensive review of the current knowledge on the formation mechanisms of severe haze in northern China [4], and in that review, the synergetic effects of anthropogenic emissions and atmospheric processes over large scales were emphasized [4].

$PM_{2.5}$ is composed of fine particles produced from various physical processes (primary emission) and gas-to-particle conversion (secondary pollution) [4]. In 2014, Huang et al. reported that secondary organic aerosol (SOA) accounted for a large fraction of the $PM_{2.5}$ mass (up to 27%), which is similar to proportion of secondary inorganic aerosol (SIA) found in field measurements made during haze episodes in four Chinese cities [5]. These and other results have shown convincingly that secondary aerosols are most often responsible for haze formation.

Chemical analyses of $PM_{2.5}$ and source apportionment studies have shown that emission controls for volatile organic compounds (VOCs) and nitrogen and sulfur oxides (NO_x and SO_x) from coal combustion, biomass burning, and motor vehicles are needed to mitigate the high PM levels in urban areas [4,5], and this is consistent with a report published in 2014 [6]. Indeed, the Chinese parliament proposed a national campaign against air pollution 'to accelerate the overall environmental initiatives and improve people's quality of life'. In early October 2012, the State Council of China formulated the Twelfth Five-Year Plan for air pollution control in key regions. The proposed plan involved stringent measures to reduce primary and secondary pollutant emissions and reinforce the general management of the many sources of pollution to improve regional air quality.

Indoor air quality can be negatively impacted by the exchange of outdoor when ambient $PM_{2.5}$ loadings are high. In addition to pollutant transfer from outdoors, outgassing from furniture, paints, construction materials, carpets, and fabrics, particularly in new or recently renovated houses with poor ventilation, can severely affect indoor air quality [7]. According to a WHO report, NO_x and VOCs, including benzene, polycyclic aromatic hydrocarbons (especially benzo[a]pyrene), trichloroethylene, tetrachloroethylene and formaldehyde, have a myriad of indoor sources, and their concentrations often exceed ranges that raise health concerns [8]. Moreover, long-term exposure to these toxic gases can have carcinogenic, mutagenic or teratogenic effects [9]. Considering that people typically spend more than 90% of their lives in indoor spaces with low air exchange rates, the adoption of effective control measures has become a critical issue [10].

Unfortunately, indoor air quality has received relatively limited attention in China, and the most recent indoor air quality standard (GB/T18883-2002) was released in 2002. Nonetheless, concerns about poor indoor air quality have increased, and the growing recognition of the problem provides an opportunity for the advancement of indoor air purifying technologies. Conventional air purifying methods often have high capital costs, and they are usually designed for harsh conditions and large areas and not suitable for the low concentrations of pollutants commonly encountered. Here, we present a comprehensive overview of current research trends involving nanotechnologies for air pollution abatement, with special reference to catalysis for the removal of NO_x, VOCs and formaldehyde. Applications of nanomaterials for disinfection are also briefly reviewed in the final section.

1.1. Major Sources of NO_x and Common VOCs

Anthropogenic, combustion-related emissions, including those from fossil fuel and biomass burning for power and heat, are the main sources for a wide array of airborne pollutants, including PM, SO_x, CO, unburned hydrocarbons, and NO_x [11,12]. Of these, NO_x is a particular cause for concern because its high photochemical reactivity in atmosphere can lead to secondary particle formation and haze, O_3 production, acid precipitation, and adverse health effects [12,13]. Furthermore, NO_2 is photochemically reactive and listed as the priority gas pollutant by the WHO due to the acute injuries it can cause to pulmonary tissues [8]. Coal-fired power plants, industrial plants (i.e., cement plants, iron-steel plants, industrial boilers and others), and motor vehicles (e.g., on-road, off-road and shipping) contributed more than 90% of total NO_x emissions [14].

Under the legislative actions of the Chinese government, starting in 2010 low NO_x burners (LNBs) were required for coal-fired plants with capacities larger than 100 MW,

and deNO_x devices were required to be installed to reduce NO_x emission [14]. Large quantities of NO_x are still being emitted from the sintering process used by iron-steel industries due to the ongoing demand for construction materials coupled with the lack of effective deNO_x systems [14]. In cement plants, rotary kilns with high temperatures also contribute to the problem, causing higher NO_x emissions than shaft kilns [14]. Motor vehicles powered by heavy fuel oil or diesel are also major contributors to NO_x emissions on a national scale, especially those using fuels containing fuel-bound N that produce more NO_2 than gasoline engines [12,15]. In the residential sector, coal burned for cooking and wintertime heating across northern China accounts for a large fraction of the NO_x emissions [4]. The scope of the NO_x problem can be seen in large number of sources that have contributed to the massive releases of NO_x into the atmosphere. In addition to anthropogenic emissions, natural sources, such as volcanic eruptions, lightning, NH_3 oxidation, and spontaneous fires, emit NO_x into the atmosphere and should be mentioned.

Except the natural sources of VOCs emission, anthropogenic VOCs emission continuously increased in China from 2000 to 2015 due to the sustained economic growth and absence of effective control measures [16]. For all sectors, solvent use, petroleum-related industries, biofuel combustion, and transportation are considered primary contributors [14]. In the petroleum industry, the exploitation, storage and transport of the liquid/gas fuel, petrol/gas stations, and petrochemical processes that use fuels as raw materials are the principal emission sources. The major sources for solvents include the out-gassing of paints used for vehicles and architectural walls, printing inks and toners, and adhesives, and releases during the production of pharmaceuticals.

As VOC emissions continue to increase, additional stringent regulations are being imposed by the Chinese government to limit the releases of organic solvents into the atmosphere. A series of national industrial standards has also been established to suppress the emissions from fossil fuel exploitation and solvent use, including wood and interior wall finishing, architecture and vehicle painting, indoor adhesives, leather and textile products, and furniture [14]. Biomass burning is the most important VOC emission source for the residential sector, and motor vehicle exhaust is the predominant source for the transportation sector [14].

VOCs include more than 300 types of the carbon-based chemicals that share the common characteristics of low boiling point, high vapor pressure, and strong reactivity [17]. The nature and types of VOCs vary widely amongst different emission sources [18]. Gasoline-powered vehicles emit negligible C10 and higher VOC species, whereas n-nonane, n-decane, n-undecane and n-dodecane are common components of diesel vehicle exhaust. The n-alkanes, n-alkenes, and aromatics are major groups found in the vehicle exhaust sources.

The VOC species of greatest concern to human health and the environment are: (1) Aldehydes, whose representative species are formaldehyde and acetaldehyde, and are often found in construction materials and plastic adhesives. Aldehydes can cause throat, eye, and skin irritation and are identified as primary carcinogens; they also are precursors of ozone [17]. (2) Aromatics, whose representative species include benzene, toluene, ethylbenzene and xylene (BTEX), are found in gasoline- and diesel-powered vehicle exhaust, petroleum products, paintings, coal and biomass burning. BTEX species are carcinogens and mutagenic to humans and pose a variety of threats to the environment, such as the depletion of ozone and the production of photochemical smog. (3) Double-bond alkenes, namely isoprene and 1,3-butadiene, which are mainly emitted from vehicle exhaust, are extremely reactive, and participate in photochemical reactions that produce ozone [18].

1.2. Conventional Control Methods for Air Pollutants

Control technologies designed for stationary and mobile sources include physical devices that remove particulate matter (or dust) and chemical processes that prevent emis-

sions of aerosol precursor gases (i.e., NO_x, SO_x and VOCs). Table 1 lists the removal mechanisms for each type of pollutant and includes remarks on treatment efficiency, advantages, disadvantages, and applications. Electrostatic precipitators, wet scrubbers, cyclones, and baghouses (or fabric filters) are commonly used for particle control [2]. Particle removal mechanisms include sieving, gravitational settling, inertial impaction, interception, diffusion, electrostatic precipitation, etc. The removal efficiencies for these approaches vary as complex functions of particle size [19]. To prevent fine particles from being emitted into the atmosphere, conventional technologies are continuously being improved, and hybrid systems with combinations of two or more methods are being developed [2].

The methods for NO_x abatement can be generally divided into in-combustion and post-combustion procedures [20]. For in-combustion methods, parameters such as reactant residence times, temperature peaks, and O_2 concentrations are adjusted to reduce NO_x formation. The use of LNBs is an approach that belongs to the in-combustion methods for stationary and mobile sources. Before 2010, only medium- (≥100 MW and <300 MW) and large (≥300 MW)-size coal-fired power plants in China adopted the LNB technology.[14] During the 2015–2016 time period, the supercritical circulating fluidized bed (CFB) combustion has become the most promising technology and series of CFB boilers have been established in 350 MW plants in China. The advantages of fluidized bed combustor, such as compact furnace design and relatively uniform temperature, guarantee the effective burning of wide ranges of fuels and significant reduction of NO_x and SO_x emissions [21,22]. The recent works have been focused on evaluation of NO_x emission from the chemical looping and calcium looping combustion processes, as they are emerging promising post-combustion technology for CO_2 capture for coal-fired burners. The fuel types and properties, flue gas oxygen feed and NO feed to the fluidizing gas are all great contributors to influence NO_x emission [23,24].

Since 2010, selective catalytic reduction and selective noncatalytic reduction (SCR and SNCR, respectively) technologies have been gradually introduced—these methods belong to the post-combustion procedures [25]. Table 1 summarizes the primary post-deNO_x methods, their principles, and performance in various applied scenarios. Although the SCR and three-way-catalysis (TWC) methods have become widely commercialized, the following problems need to be addressed: (1) high cost of the SCR technology for small-scale power plants and industrial boilers; (2) ammonia leaks—these have become a problem because NH_3 is a target of regulations; and (3) TWCs are not effective for diesel or lean-burn gasoline engines [11,12]. Under the current circumstances, large amounts of NO_x are still being discharged into the environment and continue to cause deteriorations in air quality.

The abatement of anthropogenic VOCs is especially challenging because their composition, physical properties, reactivity, and emission sources are diverse. Typical end-of-pipe VOC abatement approaches are also summarized in Table 1. Generally, VOCs can be recovered by absorption, adsorption, condensation, membrane separation, and bio-filtration, or they can be destroyed by combustion, catalytic or biological oxidation processes [26]. To address the drawbacks with adsorption and combustion, researchers have developed catalytic VOC oxidation technologies in which VOCs are oxidized using a suitable catalyst at relatively low temperatures (250 to 500 °C). The catalysts are designed for dealing with effluent streams containing low VOC concentrations. The key challenge lies in choosing the best and most robust catalyst for a variety of pollutants because of the complexity of the VOCs mixtures [26]. Biological treatments offer a cost-effective and environmental-friendly approach to decompose VOCs and the odors emitted from agriculture, farming and sewage wastewater plants [27]. Hence, no single technology can be universally used to treat gaseous pollutant mixtures that differ in composition and concentrations. Combinations of technologies are especially favorable for situations requiring extreme purification.

The current air pollution mitigation methods have not been sufficient to prevent the frequent occurrence of haze episodes in China. Emission inventory studies in China have shown that the lowest uncertainties are mainly associated with the emissions from large point sources, such as power plants, cement plants, on-road vehicles, shipping, and residential combustion. On one hand, the lack of definite emission profiles for other industries or processes increases the difficulty of source pollution control [14]. On the other hand, meeting the stringent air quality regulations imposed by the WHO and local governments (e.g., Hong Kong) will require further technological innovations. According to WHO guidelines, the annual average $PM_{2.5}$ value should be <10 $\mu g/m^3$, and the NO_x level established by EU directive for the protection of human health is 105 ppbv. Therefore, an abundance of research opportunities exists for improving current technologies and for developing novel technologies to protect the environment and human health.

Table 1. Major post-combustion control methods for particulate matter, NO_x and VOCs mitigation from sources.

Type of Pollutant	Method	Mechanisms and Usage in China	Efficiency	Advantages and Drawbacks	Applications	Reference
Particulate matter/dust	Electrostatic precipitators	Particle collection by electrostatic forces, more than 90% coal-fired power plants installed	Poor performance for $PM_{2.5}$ removal	Effective for large (>1 μm) and ultrafine (<0.1 μm) particle removal, low cost and energy consumption, affected by temperature and humidity	Coal-fired power plants, cement and metallurgy industries; household dust removal	[2,28]
	Wet scrubbers	Particle adsorption by liquid sprays, dominant technology in China	Low efficiency for $PM_{2.5}$ removal (~50%)	Simultaneous removal of some gaseous pollutants; high power consumption, metal corrosion, need for effluent treatment	Coal-fired power plants and cement industries	[2,19]
	Cyclones	Particle collection by centrifugal forces, typical pre-cleaners for large particles in most industries	Low efficiency for $PM_{2.5}$ removal	Low cost and simple structure, not recommended for $PM_{2.5}$ removal	Coal-fired power plants, cement and chemical industries	[2,19]
	Baghouse (or fabric filters)	Particle collection by filtration through porous textile fabrics, less than 10% thermal power plants installed	High efficiency for $PM_{2.5}$ removal (>99%)	High efficiency for dust, simple structure, low investment; regeneration of filter media, temperature sensitivity	Coal-fired power plants, cement and iron–steel industries	[2,29]
Nitrogen oxides	Selective catalytic reduction	Catalytic reduction by NH_3 or hydrocarbon over metal oxides at high temperatures to form N_2 and H_2O nearly 90% thermal power plants installed	High $deNO_x$ efficiency (80–90%)	High conversion rate, adaptable for high dust conditions (particulate levels 1 to 30 g/m^3), NH_3 leaks and high cost of catalysts (i.e., Pt/Al_2O_3)	Coal-fired power plants, cement and iron–steel plants, industrial boilers, diesel engines	[26]
	Selective non-catalytic reduction	Reduction by NH_3 or aqueous urea at very high temperatures (850 to 1100 °C), nearly 90% thermal power plants installed	Low $deNO_x$ efficiency (30–75%)	Simplicity; catalyst free; low capital and operational costs; NH_3 leaks, high temperature and narrow temperature window	All types of stationary fired equipment	[13]
	Three-way catalyst	Conversion of CO into CO_2 and NO_x into N_2 and O_2 over a catalyst surface	High $deNO_x$ efficiency (>95%)	High efficiency; high cost of catalysts (i.e., Pt/Rh/Pd); not suitable for diesel engines	Gasoline-powered motor vehicle engines	[30]

	Adsorption (combined with condensation or recovery)	Gas adsorption over zeolite and carbonaceous material (activated carbon, biochar, carbon nanotube and grapheme); widely used	High efficiency (>90%)	Economical, recover useful solvents, suitable for highly diluted exhaust gas stream with large volume; high regeneration cost and secondary pollution due to desorption	Petroleum-related industries, chemical industries, packing and printing industries, spraying and painting in car industries and indoor environments	[18,31]
Volatile organic compounds	Regenerative thermal oxidation	Incineration at extremely high temperatures (>1000 °C); widely used	High efficiency (>99%)	High efficiency in removing VOCs from flue gas streams with high flow rates and high VOC concentration; high energy consumption; undesirable by-products, such as dioxins and CO; possible explosion	Petroleum and coke industries, chemical industries, printing industries, spraying and painting industries, pharmaceutical plants, textile industries	[26]
	Regenerative catalytic oxidation	Catalytic oxidation over noble metals or non-noble metal oxides at moderate temperatures (250 to 500 °C), widely used	High efficiency (>99%)	Energy efficient, suitable for dilute effluent streams of VOCs (<1% VOCs) with moderate flow rates, lower formation of dioxins and by-products, high cost of catalysts and catalyst deactivation	Printing industries, spraying and painting industries, pharmaceutical plants, textile industries, petroleum and coke industries	[26]

2. Ambient Air Purification by Nanotechnologies

Recent developments in nanotechnology have led to exceptional opportunities in the use of nanomaterials for environmental remediation. Compared with bulk materials, nanomaterials have larger surface areas and show remarkably different electronic, magnetic, and catalytic properties for PM < 100 nm, which make them superior for filtration, adsorption and photocatalysis [20,31,32,33]. We discuss below the basic principles for ambient air purification with nanomaterials (APN), especially in relation to air pollutants at low concentrations (sub-ppb to ppm range), low emission intensities, and from dispersed sources. These applications take advantage of the special properties of the nanomaterials, including quantum confinement and surface/interface effects.

Nanomaterials can be used for particle filtration, gas adsorption, bacteria disinfection and catalytic processes; and they have been components of various types of purification devices used to reduce particulate matter (PM), gaseous precursors (i.e., NO_x, VOCs, etc.), and toxic pollutants (e.g., HCHO), as shown in Figure 1. Advantages of nanomaterials include moderate working conditions, no burdensome instrumental set-up, and low operating costs. Indeed, the APN technology often can be an ideal solution for improving the air quality in residential and urban areas, and it is especially well suited for applications in confined environments. As a result of these advantages, a substantial budget was allocated by Chinese government for research on nanomaterials and APN technology for pollution abatement, and APN will undoubtedly receive increased attention throughout the world in the future.

Here, our objective is to present a comprehensive overview of APN technology from fundamental theory to real world air purifying applications. The specific topics to be discussed include (1) the development of novel nanofibrous filters for fine particle collection in low pressure-drop systems; (2) improvements in aerosol precursor gas adsorption and degradation kinetics from the perspective of nanomaterial design and parameter optimization; (3) a review of the fundamental mechanisms of photocatalytic and ambient temperature catalytic degradation of gas pollutants, including reaction pathways and key intermediates; and (4) a summary of developments in nanomaterial immobilization and purifying modules as applied in field-tested techniques. Finally, we show how control systems based on APN technology can offer a path forward for protecting the general public from severe air pollution.

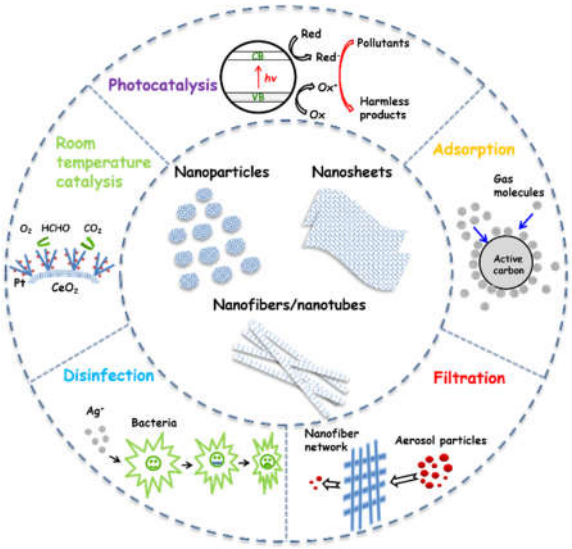

Figure 1. Technologies used for ambient air purification by nanomaterials.

3. Filtration

"The past experiences in the cities in the USA and recent data obtained by the Institute of Earth Environment in Xi'an, China indicated that it might take a decade or longer for particle filtration to be reduced to an acceptable level" [2]. Although regulations on $PM_{2.5}$ emission from industries and vehicles recently have been strengthened in China, adverse health effects remain a significant concern. Membranes/filters, including those made from electrospun nanofibers, have gained wide acceptance for applications in $PM_{2.5}$ collection owing to their superior filtration efficiency and low pressure drop.

Conventional filtration is effective for capturing large pollutant particles, but in practice, that approach has some significant pitfalls including frequent fouling, high energy use, and high operating costs. Unlike conventional multilayer air filters, electrospun nanofiber mats are characterized by high porosity and micrometer-sized void spaces, resulting in low resistance to airflow and low pressure drops [32,34]. High-power pumps are not needed for these materials.

Filtration performance is not only affected by pressure drop but also by filtration efficiency. Increasing the polarity and surface electrostatic charges of the polymers used to make nanofibers are common strategies for improving their filtration efficiency [32,35]. Several special functionalities can also be added to nanofibers by incorporating active components into the polymers used to make them. For example, as iron oxide accounts for a large fraction in the airborne dust, magnetic metal oxide nanoparticles (Fe_3O_4) can be added to electrospun nanofibers to attract dust through magnetic attraction (Figure 2a,b) [36].

The simultaneous capture of aerosols and formaldehyde can be achieved with high efficiency (95%) at a low pressure drop (112 Pa) with composite polyacrylonitrile (PAN)/β-cyclodextrin nanofiber membranes.[37] Dan Lv et al. [38] developed a multipurpose air filter made up of ZnO nanoparticles, polyvinyl alcohol, and konjac glucomannan-based nanofiber membranes. This type of filter exhibited superior filtration performance (>99.99%) for ultrafine particles compared with commercial HEPA filters; moreover, the flow resistance of the filters was low, and they displayed excellent photocatalytic and antibacterial activity functions.

In another study, a triboelectric nanogenerator (TENG) was incorporated into a self-powering air filter made of electrospun polymer-coated stainless-steel wires. This type of device, when combined with a photocatalytic active component, showed remarkable performance in terms of $PM_{2.5}$ capture and formaldehyde decomposition.[33] For real-life applications, face masks and window materials made of nanofiber-loaded nonwoven fabrics have been developed to protect public health and to prevent outdoor $PM_{2.5}$ from entering indoor spaces (Figure 2c,d) [32,34]. There is good evidence that polymer-derived nonwoven nanofiber mats are suitable for environmental use due to their lightweight and tolerance of high-temperatures. In particular, ceramic nanofibers, specifically γ-Al_2O_3 nanofiber membranes, with excellent thermal and chemical stabilities, are suitable for treating vehicle exhaust and for industrial filtration applications [34].

To develop efficient and stable air filtration devices, the mechanisms by which electrospun nanofibers capture PM need to be understood. In situ optical microscopy is a common way to study these processes [32], and studies of that type have shown that small PM quickly aggregates to form large spherical particles once they are captured by nanofibers. This is especially true for the points where the nanofibers join because large PM aggregates tend to accumulate there. Figure 2e,f clearly show that smoke PM formed a coating layer strongly wrapped around each nanofiber. These observations provide insights into how the effects of particle size and shape and surface properties of the polymer nanofibers affect filtration performance.

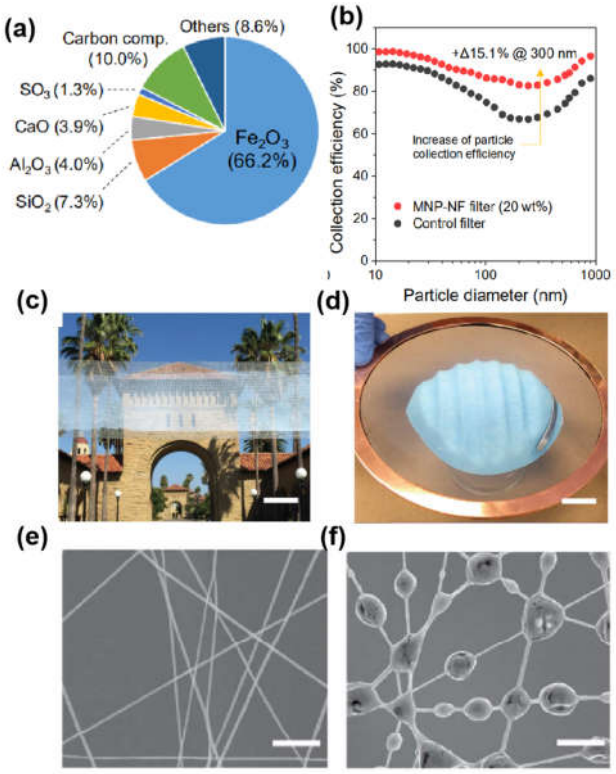

Figure 2. (**a**) Chemical composition of dust from a subway station in Seoul, South Korea. (**b**) Comparison of subway dust collection efficiency for a control filter versus a 20 wt % Fe_3O_4 nanoparticle-NF filter. (**c**) Photograph of a roll-to-roll produced transparent air filter. Scale bar is 5 cm. (**d**) Photograph showing that freestanding nanofiber film can be easily transferred onto a facemask. Scale bar is 3 cm. (**e**,**f**) SEM images of Nylon-6 nanofibers before and after filtration. Scale bars in (**e**,**f**) are 2 μm. (**a**,**b**) Reprinted with permission from the reference [36]. (**c**–**f**) Reprinted with permission from the reference [34].

4. Adsorption

Adsorption is a non-destructive process that can be used to remove gaseous pollutants from air under ambient conditions, and there are two different processes, physisorption (non-covalent) and chemisorption (covalent), that may be involved. Sorption capacity largely depends on the following: (1) the physical structure and chemical composition of the sorption materials, including their specific surface area; (2) pore size/distribution and surface functional groups; (3) molecular structure, polarity, acidity and wettability of the target pollutants; and (4) adsorption conditions, principally temperature and humidity [18,39]. For NO_x removal, Gomez-Garcıa et al. [12] showed that metal oxides, spinels, perovskites, zeolites, carbonaceous material, and heteropolyacids are primary sorbing materials with high capacities for uptake. Transitional metal (Co, Cu, Ni, Fe and Mn) oxides were found to have the best NO uptake because covalent bonds formed between the metal ions and NO [40–42]. In contrast, rare earth and alkaline earth metals, such as Ce, La, Ba and Na, showed comparatively low NO adsorption [12]. Zeolite exchange with transitional metal ions, and carbonaceous materials modified with iron or copper oxides also exhibited excellent NO uptake performance.

For VOC removal, carbonaceous materials of various forms are the most commonly used adsorbents [18]. Activated carbon (AC) is the most popular of these, and AC is widely used for gas sorption, with applications for alkanes, alcohols, ethers, aldehydes, and aromatics. However, due to its microporous (pore size ≤2 nm) and disordered pore structure, the movements of large VOC molecules are inhibited, and that results in slow

adsorption kinetics [43–45]. Compared with AC particles, AC fibers (ACFs) with essentially a 1D structure are a novel material that exhibits fast adsorption kinetics due to the presence of short and straight micropores [28,46]. The ACFs also show unique adsorption behavior for nonpolar or weakly polar VOCs, such as toluene and formaldehyde, due to their nonpolar nature and lack of surface O groups. Furthermore, thermal treatments, acid treatments, or metal oxide modifications can be used to add oxygen functional groups to the ACFs which enhances the removal of polar VOCs [47]. ACFs are a promising candidate for commercial gas adsorption applications because they can be made into fabrics or other desired self-supporting forms.

With the advancement of nanotechnology, 1D carbon nanotubes and 2D graphene (oxidized and reduced states) nanosheets have become used for electronics, catalysis, photonics, and environmental remediation [48–50]. The extremely large surface areas (up to 3502.2 m^2/g) of these nanomaterials has led to increased demands for their use in high capacity VOC adsorption applications compared with traditional AC [50,51]. Another advantage of nanomaterials made of graphene oxide is that the abundance of the surface oxygen functional groups facilitates the adsorption of the hydrophilic VOC molecules, but a drawback is that the aggregation of graphene oxide has severely restricted their commercial utilization as adsorbents.

Nonetheless, graphene oxide can be processed into various self-supporting forms or used as a supporting material for dispersed catalysts designed for simultaneous VOC adsorption and degradation [52,53]. Other carbonaceous materials, such as biochar and ordered mesoporous carbon, also have been investigated for use as VOC adsorbents [18]. Previous studies and reviews have shown that significant progress has been made in the control of VOCs with these materials [39,45,49,51,52], but the development of low-cost, high-efficiency (under a range of humidity conditions) and easily recyclable adsorbents remains a challenge for their applications in pollution control.

5. Photocatalysis

Nanomaterial-driven photocatalysis provides a green solution for removing air pollutants in the atmosphere. Early in 1986, Takeuchi and Ibusuki found that metal oxides in atmospheric PM played critical roles in the photochemical catalytic conversions of hydrocarbons and NO_x. These are reactions that strongly enhance the formation of CO_2 and HNO_3 and decrease O_3 [54,55], and several photoactive metal oxides, including TiO_2, ZnO and Fe_2O_3 can be relatively abundant in the atmosphere, and heterogeneous reactions catalyzed by these photoactive materials have been considered for removing pollutants from the air.

Although photocatalysis has been studied for more than 40 years, water splitting for H_2 and wastewater treatment is still far from commercially viable due to the low energy conversion efficiency and complicated procedures for recycling photocatalysts. By contrast, significant numbers of patents issued for photocatalytic air purification reflect a growing interest in the adaptation of this approach for air quality applications [56]. Japan and several countries in the EU have pioneered basic research in this area and conducted field studies on the photocatalytic removal of air pollutants, whereas China has only recently started to focus on this field. In this section, photocatalysis principles, strategies for optimizing nanomaterials, effects of environmental conditions, reaction mechanisms, and nanomaterial immobilization are discussed in detail.

5.1. Principles of Photocatalysis and Major Nanomaterials

Photocatalysis is an advanced oxidation process (AOP) that involves irradiated semiconductors and causes not only the rate, but also the direction of a chemical reaction to be altered. In Fujishima–Honda energy band theory,[57] one electron (e^-) is excited from the valence band maximum (VBM) to the conduction band minimum (CBM) by absorbing one photon with sufficient energy, thereby simultaneously leaving a positive hole (h^+) in

the valence band (Equation (1)). Photogenerated e^--h^+ pairs achieve spatial separation from surface reaction sites by diffusion or migration.

Once they have arrived at the photocatalyst surface, excited charge carriers can react with the pre-adsorbed H_2O and O_2 to produce reactive oxygen species (ROS), such as hydroxyl (Equation (2)) and superoxide radicals (Equation (3)). These radicals possess extremely strong oxidation potentials, barely showing any selectivity towards pollutants, thereby enabling the complete conversion of the gaseous pollutants into harmless products. It is important to note that the ability to produce ROS and their oxidation and reduction capacities are mainly determined by the respective VB and CB positions of a specific photocatalyst. Figure 3 presents the band positions of some semiconductors and their relative position with the redox level of •OH and $\bullet O_2^-$ formation.

$$\text{Photocatalyst} + \text{hv} \rightarrow h^+ + e^-, \quad (1)$$

$$h^+ + H_2O \rightarrow \bullet OH + H^+, \quad (2)$$

$$e^- + O_2 \rightarrow \bullet O_2^-, \quad (3)$$

The semiconductor photocatalysis principles related to environmental pollutant purification are also illustrated in Figure 3. As shown, the overall photocatalytic efficiency of the functional nanomaterials is determined by light absorption efficiency ($\eta_{abs.}$), charge separation efficiency ($\eta_{sep.}$) and most importantly, the surface reaction efficiency ($\eta_{rea.}$), as follows (Equation (4)):

$$\eta = \eta_{abs.} \times \eta_{sep.} \times \eta_{rea.} \quad (4)$$

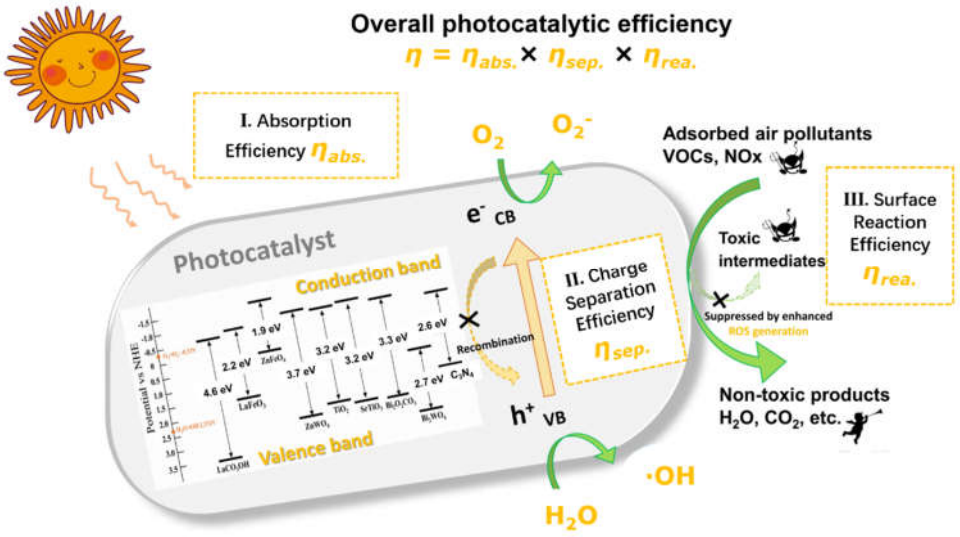

Figure 3. Scheme of environmental remediation principle by semiconductor photocatalysis.

Various semiconductor nanomaterials have been employed for use in photocatalytic reactions; these include TiO_2, ZnO, WO_3, Fe_2O_3, $SrTiO_3$, $BiVO_4$, Bi_2WO_6, BiOX (X = Cl, Br, I), *g*-C_3N_4, etc., which can have different phases, morphologies, and modifications [58]. To improve the efficiency of each elementary step, various strategies have been used to modify the physicochemical properties of nanomaterials. For example, element doping (metal or nonmetal) to induce impurity states in wide bandgap semiconductors has been used to extend the light absorption range, while plasmonic noble metal (Ag and Au) deposition is a popular way to enhance light absorption and inhibit photoinduced charge recombination [59,60].

The construction of binary or ternary composites to form heterostructured interfaces has been widely used to promote charge separation and enhance light absorption. Facet modulation and oxygen vacancy engineering have become widely used for interfacial charge transfer enhancement [61,62]. Porous metal-organic-frameworks were also adopted to enhance gas adsorption to facilitate the photoreaction [63]. In Table 2, we highlight some recent emerging photocatalysts that have been used for the decomposition of gaseous pollutants and summarize their synthesis strategies, reaction conditions and performance.

Table 2. Summary of typical nanomaterials used for gaseous pollutant photodegradation.

Photocatalyst	Synthesis	Reaction Conditions			Performances	Reference
		Target Pollutant	Initial Concentration	Light Source		
B-Doped g-C_3N_4	Hydrothermal reaction and calcination in N_2	NO	400 ppb (continuous flow mode)	300 W Xenon lamp (λ > 420 nm)	NO removal efficiency (30.4%)	[64]
Ag-AgBr-TiO_2	Stirring under room temperature	Benzene and acetone	250 ppm (fixed-bed mode)	Visible light (λ > 400 nm)	Removal efficiency: benzene (47.2%) acetone (70.4%)	[59]
Au-TiO_2	Calcination in air	HCHO	50 ± 2 ppmv (continuous flow mode)	Visible light	Conversion rate: 83.3% (RH = 44.0%)	[60]
F-TiO_2/Pt	Photodeposition for Pt and NaF soaking (pH = 3.5) for surface fluorination	Toluene	50 ppmv (closed reactor)	370 nm UV light	Removal efficiency: 53.0% (after the fifth cycle)	[65]
Carbon nanodots/$ZnFe_2O_4$	Hydrothermal reaction	NO	400 ppb (continuous flow mode)	Visible light (λ > 420 nm)	Removal efficiency: 38.0%	[66]
Bi/$ZnWO_4$	Hydrothermal reaction	NO	400 ppb (continuous flow mode)	Visible light (λ > 420 nm)	Removal efficiency: 63.0%	[67]
$CuInS_2$/Bi_2WO_6	Solvothermal and hydrothermal synthesis	Toluene	1 μL (fixed-bed mode)	Visible light (λ > 420 nm)	Removal efficiency: 63.0%	[68]
$Bi_2O_2CO_3$/$ZnFe_2O_4$	Hydrothermal reaction	NO	400 ppb (continuous flow mode)	Visible light (λ > 420 nm)	Removal efficiency: 32.0%	[69]
Ag-decorated WO_3/Bi_2WO_6	Hydrothermal reaction	Chlorobenzene	2 μL in a closed 120 mL reactor	Xe lamp	Removal efficiency: 80.0%	[70]
BiOCl (001) and (010)	Hydrothermal reaction	NO	600 ppb (continuous flow mode)	Visible light (λ > 420 nm)	Removal efficiency: BiOCl (001): 50.1% BiOCl (010): 60.4%	[61]
(001) TiO_2 nanotubes	Electrochemical anodization and NaF treatment	Toluene; HCHO; Aldehyde	10 ppmv (closed reactor)	370 nm UV light	Removal efficiency: toluene (32.7%) HCHO (97.2%) aldehyde (58.7%)	[62]

Sr-doped defective TiO_2	Hydrothermal reaction	HCHO	1 ppm (continuous flow mode)	UV light (λ = 365 nm, 90 mW cm^{-1})	Removal efficiency: 50.85%, QE: 5.53%	[71]
Er^{3+}-Doped TiO_2	Sol-gel method	Acetaldehyde; o-xylene; ethylene	o-xylene and ethylene (25 ppm flow mode); acetaldehyde (25 and 500 ppm flow mode)	Visible light (λ > 420 nm)	Removal efficiency: Acetaldehyde (99.2%) o-xylene (84.6%) ethylene (22.4%)	[72]
Graphene-TiO_2 composite mats	Hydrothermal reaction and Electrospinning method	Gas-phase methanol	4000 ± 200 ppm (static mode)	UV light	Removal efficiency: 100%	[73]
Fe-based metal-organic-frameworks	Solvothermal method	Toluene	460 ppm (closed-circulation reactor)	Simulated sunlight (100 mW cm^{-2})	100% adsorption and photodegradation removal efficiency	[63]
Core-shell CeO_2@LDHs	Reverse precipitation and hydrothermal method	Formaldehyde	8.0, 16.0, 24.0, 32.0 and 40.0 mg m^{-3} (continuous flow mode)	Visible light	Removal efficiency: 86.9%	[74]

5.2. Key Aspects Underpinning Photocatalytic Efficiency

5.2.1. Light Absorption

Light-harvesting ability of a photocatalyst governs the wavelength and number of photons it can utilize to trigger chemical reactions. Traditional metal oxides and oxyhalides, such as TiO_2, ZnO, $SrTiO_3$, and BiOCl are wide bandgap (Eg >3.0 eV) semiconductors that only respond to ultraviolet (UV) light with wavelengths <400 nm. However, UV light only accounts for a small fraction, 3–5%, of the entire solar spectrum [75–77]. To expand the light absorption range, researchers have developed techniques for element doping (metal or non-metal) into bulk semiconductor lattice structures to induce the formation of the interband hybrid energy levels that enable charge excitation by photons with lower energies [78–80]. For example, Wang et al. [64] prepared B-doped nanotubular *g*-C_3N_4 which had an enhanced NO removal rate compared with its undoped counterpart (Figure 4a). On the contrary, Pichat et al. [81] observed that Cr-doped TiO_2 expanded light absorption region into visible light and considerably decreased photocatalyst oxidation activity, and that was attributed to Cr^{3+} impurity states facilitating electron-hole recombination. Conflicting statements about the effectiveness of element doping abound in the literature, and those discrepancies often have been due to inaccurate controls on the doping process or other problems with the investigations.

Noble metal nanoparticle (i.e., Ag and Au) deposition with unique surface plasmon resonance (SPR) properties has become a popular method for broadening the visible light utilization of wide bandgap semiconductors [82,83]. Unfortunately, the high price and scarcity of the noble metals restrict real world applications in environmental management; indeed, more cost-effective and stable photosensitizers need to be developed. Carbon nanodots (CDs) are biocompatible and inexpensive photosensitizing materials notable for their up-conversion photoluminescent properties; that is, they can convert long wavelength light to shorter wavelengths [66,84,85]. For instance, Liu et al. observed that CDs harvested near-infrared light (≥600 nm) and then fluoresced at shorter wavelengths to excite TiO_2 nanosheets for surface reactions [86].

The intrinsic photosensitizing mechanisms for CDs are still not completely understood because the electronic structures of CDs are complex, and the CDs can act as either electron donors or acceptors [87]. Recently, non-noble metal Bi nanoparticles have been reported to induce surface plasmon resonance [88]. Gao et al. also fabricated Bi nanoparticle-anchored $ZnWO_4$ microspheres, which showed robust photocatalytic ability for ppb-level NO removal under visible light irradiation (Figure 4b) [67]. Further improvements in the utilization of visible solar energy will be needed for practical applications of CDs to environmental cleaning-up. Ideally, the catalysts ultimately chosen also should be green, inexpensive, and durable.

5.2.2. Charge Separation

Upon illumination, excited e^-/h^+ pairs in semiconductors can be generated on time scales of femtoseconds (fs). Then, the time needed to initiate surface reactions between surface charges and adsorbed substrates takes several nanoseconds to milliseconds. However, photoexcited e^-/h^+ recombination occurs within picoseconds and that is more rapid than the charge migration and transfer kinetics [89]. Therefore, charge carrier recombination is highly undesirable because the solar light energy is wasted, resulting in poor efficiency. Hence, remarkable efforts have been devoted to the engineering and synthesis of unique nano-structures that can facilitate e^-/h^+ pair separation.

For bulk semiconductors in a space-charge depleted state, the internal electric fields drive electrons and holes apart. As a representative example, layered *g*-C_3N_4 shows improved photocatalytic activity due to a stacked interlayer electric field which facilitates photogenerated carrier separation [90]. Li et al. [91] increased the internal electric field magnitude of Bi_3O_4Cl nanosheets by regulating the percentage of (001) facet exposure. In

forming electric fields, the construction of p–n or n–n heterojunctions is a popular strategy for enhancing interfacial charge separation [92–95]. As shown in Figure 4c, the p–n heterojunction interface is constructed between $ZnFe_2O_4$ (p-type) and $Bi_2O_2CO_3$ (n-type). To achieve Fermi level equilibrium, the band positions of $ZnFe_2O_4$ tend to move upward while those of $Bi_2O_2CO_3$ tend to move downward, so that the electric field is formed at the heterojunction interface, which promotes photogenerated e^-/h^+ separation under illumination [69].

Some heterojunctions with intimate contact can be craftily constructed in a one-step procedure. For example, Wang et al. reported the synthesis of $Bi_2O_2CO_3$/g-C_3N_4 and g-C_3N_4/$LaCO_3OH$ layered heterojunction nanomaterials through a one-step hydrothermal method using g-C_3N_4 itself as precursor to provide CO_3^{2-} [93,94]. The intimate contact between heterostructure components ensures excellent charge separation and strong photocatalytic activities for the degradation of gaseous NO under visible light.

5.2.3. Surface Adsorption Properties

Given the typically low pollutant concentrations (sub-ppb to ppm level) in the atmosphere and the requirement for water vapor and O_2 adsorption for the production of ROS, it is instructive to consider surface adsorption properties at the molecular level. As more pollutant molecules become adsorbed onto a photocatalyst surface, the reaction probability between ROS and adsorbed pollutants increases, and this is favorable for photoinduced charge separation. Several approaches have been shown to effectively improve substrate adsorption; the first of these is to choose a nanomaterial surface with specific sorption sites for targeted molecules or to create those sites by surface modification. For example, $LaFeO_3$ perovskite oxide exhibits specific chemisorption towards NO due to the empty states in the Fe 3*d* orbital [96].

A second approach is to tune the exposed facets of the nanomaterials that come into contact with pollutant molecules. This is effective because the atomic arrangements and coordination can vary among different facets, thereby leading to variations in adsorption behavior [61,69]. Third, the oxygen vacancies (OVs) of the metal oxide nanomaterials possess abundant localized electrons—this endows the material surface with enhanced ability to activate adsorbed H_2O and O_2, thereby promoting ROS generation and degradation efficiency [97,98]. An example of this is the work of Zhang et al. [86] who introduced OVs in a $SrFe_xTi_{1-x}O_{3-\delta}$ photocatalyst and showed that the modification led to enhanced O_2 adsorption and activation for ROS generation (Figure 4d).

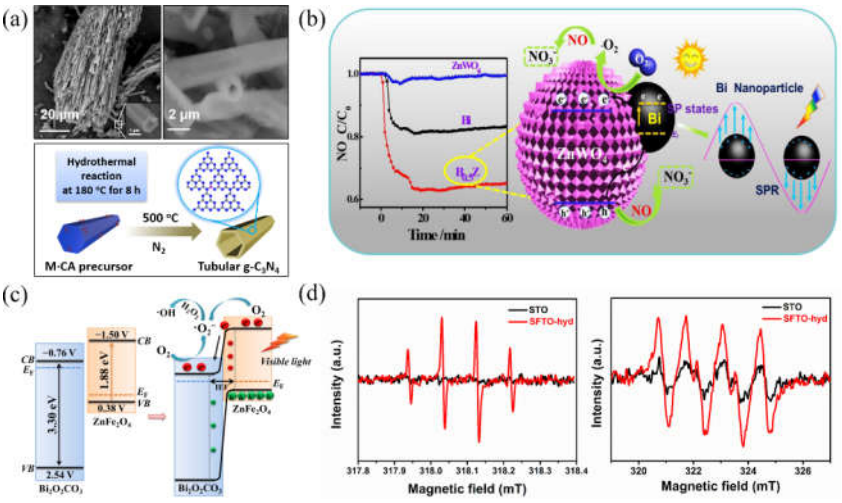

Figure 4. (**a**) B-doped graphitic carbon nitride hollow tubes. Reprinted with permission from the reference [64]. (**b**) Bi metal-induced surface plasmon resonance SPR effect with enhanced visible light ability. Reprinted with permission from the reference [67]. (**c**) Schematic illustration of e^--h^+

separation under the influence of the internal electric field of a p–n heterojunction photocatalyst under light irradiation. Reprinted with permission from the reference [69]. (**d**) Oxygen vacancy OV-enriched $SrFe_xTi_{1-x}O_{3-\delta}$ demonstrated enhanced O_2 adsorption activation ability for reactive oxygen species ROS generation. Reprinted with permission from the reference [98].

In addition to the direct modification of surface adsorption properties, combining porous and inert materials featuring large specific surface areas is another feasible approach for promoting gas adsorption. Materials such as silica [99], alumina [100], zeolites [101], grapheme [102], and AC [103,104] all offer practical support matrices. Of all supporting materials, AC is the most commonly used due to its low price, extremely porous structure, and large surface area. An increased adsorption of air pollutants onto the AC phase followed closely by mass transfer to the catalyst sites provides for efficient photodegradation and adsorbent regeneration [105].

5.2.4. Effects of Environmental Conditions

The overall reaction performance of photocatalysts can be influenced by environmental factors except for the physicochemical properties of the materials themselves. Here, light conditions, initial contaminant concentrations, relative humidity (RH) and coexisting pollutants are discussed in relation to their effects on reaction performance.

(1) Light intensity

The effects of external light intensity on photocatalysis are closely correlated to charge carrier generation, which plays a key role in photocatalytic efficiency and quantum yield. Behnajady [106] found a positive correlation between light intensity and final pollutant removal rate in a study with a well-tested model supported with experimental data. In contrast, a study by Stafford et al. [107] suggested that surface reactions occurred even at low light intensities, because the slow rate of the photoinduced hole generation caused intermediate species to reach adsorption equilibria on the catalyst surface, thereby ensuring the presence of active sites to be occupied by pollutant species. Similarly, Ohko et al. [108] found that the quantum yield increased gradually with decreasing light intensity in the photocatalytic decomposition of gaseous 2-propanol. The quantum yield in that study reached a maximum value even when the light intensity was extremely low.

More generally, the adsorbed concentration and light intensity in photocatalytic reactions are governed by the first-order kinetics (Equation (5)) as follows [109]:

$$r = \kappa \Gamma I^{\alpha}, \quad (5)$$

Here, r is the reaction rate, k is the first-order rate constant, Γ is the concentration per unit real surface area and I is the light intensity. Under light-sufficient conditions, the α value is between 0 and 1 [110].

(2) Pollutant concentration

Due to the kinetic constraints, photocatalysis alone is usually not effective for treating high pollutant concentrations, and even in the ppb and ppm ranges, pollutant removal rates can be quite variable. At low concentrations (<1 ppm), adsorption rates are slower than photo-oxidation rates, and in those cases, mass transfer is the rate determining step. When the pollutant concentration increases to a high level (ppm range), photooxidation becomes the more important rate determinant. Moulis and Krysa [111] observed that removal efficiency was high at low initial concentration of contaminants for all VOCs studied (including n-hexane, n-butyl acetate and toluene) because the surface adsorption capacity of the photocatalysts was not limited by the number of active sites [112].

Along these lines, Mo et al. [113] found that the photodegradation efficiency for toluene decreased by ~30% when its initial concentration increased from 1 to 4 ppm. Thus, after the maximum capacity of the photocatalyst has been reached, any further increments in the pollutant concentrations do not improve the performance. Nonetheless, high con-

taminant concentrations can result in enhanced reaction kinetics when the rate-determining step is controlled by mass transfer. Photocatalysis is especially well-suited for the abatement of indoor and ambient air pollutants that are in the ppb to sub-ppm concentration range.

(3) Relative humidity

Compared to other parameters, the RH effect (or water vapor level) is significant and complex because the water vapor concentrations in the air are in the thousand ppm range, which is almost always much higher than that of gaseous pollutants, and as a result, competitive adsorption exists. Moreover, the presence of water vapor is extremely important because hydroxyl radicals, one of the dominant ROS species, can be directly generated by H_2O interactions with photoinduced h^+. On the other hand, in the absence of water vapor, the photocatalytic mineralization of the pollutants evidently can be inhibited. The photocatalysis of toluene oxidation has been evaluated for dry and wet conditions in a study by Debono et al. [114], and it was shown that toluene conversion to CO_2 was favored by wet conditions.

The optimal RH value can vary among pollutant types, that is, hydrophilic or hydrophobic VOC molecules may be affected differently. In gas-phase chlorobenzene removal, for example, RH is positively correlated with the adsorption and reaction processes, and the photocatalytic oxidation rate can remain stable even at high RH (over 80%) [115]. On the other hand, it has been shown that a relatively high water vapor level inhibited acetone photocatalytic oxidation [116], and more generally, the effect of RH can vary for different photocatalyst surfaces. For 1-butene photooxidation, Cao et al. [117] found that SnO_2 was extremely sensitive to RH effects and showed a significant negative relationship between RH and the photocatalytic oxidation rate. Meanwhile, TiO_2 films maintained stable performance under identical test conditions. The RH level also affects the generation of intermediates as illustrated in a study by Sleiman et al. [118] who showed that RH is a key factor in the photocatalytic oxidation of toluene. At low RH or in the absence of water vapor, a high level of mineralization (~90%) can be achieved, but several toxic by-products are produced and accumulate simultaneously.

(4) Coexisting pollutants

In practice, air purification inevitably involves multiple pollutants with different polarities, molecular sizes, hydrophilicities, and chemical reactivities; and one substance can either promote or inhibit the removal rate of others in such complex systems [119]. For example, in the photocatalytic degradation of formaldehyde, the presence of NO promotes formaldehyde conversion, whereas SO_2 inhibits it because SO_4^{2-} ions can bind to the formaldehyde adsorption sites on the catalyst surface [120]. Indeed, competitive adsorption kinetics and interactions among individual components are thorny issues that are encountered when dealing with coexisting pollutants.

For instance, Galli et al. [121] investigated the photocatalytic oxidation of 17 types of molecules in a mixed system and found that the gas molecules competed for adsorption sites on the catalyst surface according to their polarity and initial concentration. Similarly, Debono et al. [122] studied the photocatalytic oxidation of a mixture of toluene, decane, and trichloroethylene, and they found that several reactive chlorinated species were produced when trichloroethylene was undergoing degradation, thereby affecting reaction kinetics. These studies indicate that a single photocatalyst probably will not be able to treat all types of gaseous pollutants, and therefore, it would be advantageous to develop composite nanomaterials that are effective against an array of them.

5.3. Generation of Intermediates, Catalyst Deactivation, and Regeneration

Ideally, the final products of photocatalytic pollutant decomposition should be nontoxic, innocuous, and not cause secondary pollution. Given the slow kinetics of the charge transport and interfacial charge transfer, however, the formation of intermediates and by-

products is almost inevitable. Moreover, toxic intermediates can accumulate on the surface of functional nanomaterials, occupy the active reaction sites, and consequently lead to a degradation in performance. For instance, Cao et al. [123] reported acute deactivation of TiO_2 during toluene photocatalytic degradation, and that was attributed to intermediates from incomplete oxidation, such as benzoic acid and benzaldehyde, that accumulated on the catalyst surface.

Gas chromatography-mass spectrometry (GC-MS) and in situ DRIFTS characterizations are techniques commonly used to study intermediate species formed over catalyst surfaces used for the degradation of VOCs and NO_x. However, the mechanisms that govern selectivity and that cause the generation of toxic intermediates and by-products have not been fully established. To avoid the generation of toxic intermediates, researchers have investigated the deposition of metal oxides on catalyst surfaces to change the reaction pathways [123–126]. For example, Cui et al. applied in situ DRIFTS to probe the NO photoconversion route to NO_3^- by depositing SrO clusters on a *g*-C_3N_4 surface, and it was shown that SrO facilitated NO activation via Sr-NOδ(+) formation [125]. Similarly, Li et al. employed GC-MS to show that dibenzothiophene over H_2O_2-assisted hydrothermal synthesis of TiO_2-SiO_2 was initially photocatalytically oxidized to sulfoxides, then further oxidized to sulfones. That sequence optimized selectivity in a diesel-based photocatalytic-adsorptive desulfurization process [127].

In terms of preferred reaction pathways for photocatalysis, the generation of sufficient ROS in photocatalysis is generally considered an effective method for suppressing unfavorable intermediates, and this is normally realized by the strategic design of the photocatalysts. For example, Li et al. constructed a photocatalyst with Bi@$Bi_2O_2SiO_3$ that accelerated the transformation of the intermediate N_2O_4 to the final product NO_3^-. That approach was effective because the co-existence of OVs and Bi metal had synergistic effects on ROS generation [126]. Besides, the geometric structures of ROS may also result in selectivity for photocatalytic reactions. In fact, a recent study showed that well-designed BiOCl(001) with surface OVs favored the formation of side-on superoxide radicals that could completely oxidize NO to nitrate (O_2^- B+ NO(g) → NO_3^-) without any barriers, as shown in Figure 5a [128].

Air pollutants exhibiting different adsorption activations on varied facets can also induce differences in photocatalytic conversion routes. For instance, different NO adsorption activation patterns on the (110) and (001) facets of $Bi_2O_2CO_3$ essentially predetermine the facet-dependent photocatalytic conversion pathways of NO oxidation (Figure 5b) [129]. With sufficient localized electrons, NO and corresponding toxic intermediates can be depleted or easily activated as has been verified in the work of Dong et al. [130] For open structures that facilitate O_2 diffusion, such as TiO_2 nanotubes, the formation of intermediates during the photocatalytic degradation of VOCs can be inhibited by supplying sufficient O_2. This method is also considered as a practical strategy for avoiding photocatalyst deactivation [131].

Photocatalyst regeneration is another extremely important consideration for practical applications in air purification because selectivity and stability need to be optimized to achieve safe and long-term photocatalytic air purification. In most cases, catalysts partially recover their activity after thermal treatment at high temperatures [132,133]. Sonication and UV irradiation, combined with H_2O vapor or H_2O_2 can also help the catalysts regain their original activity [133,134].

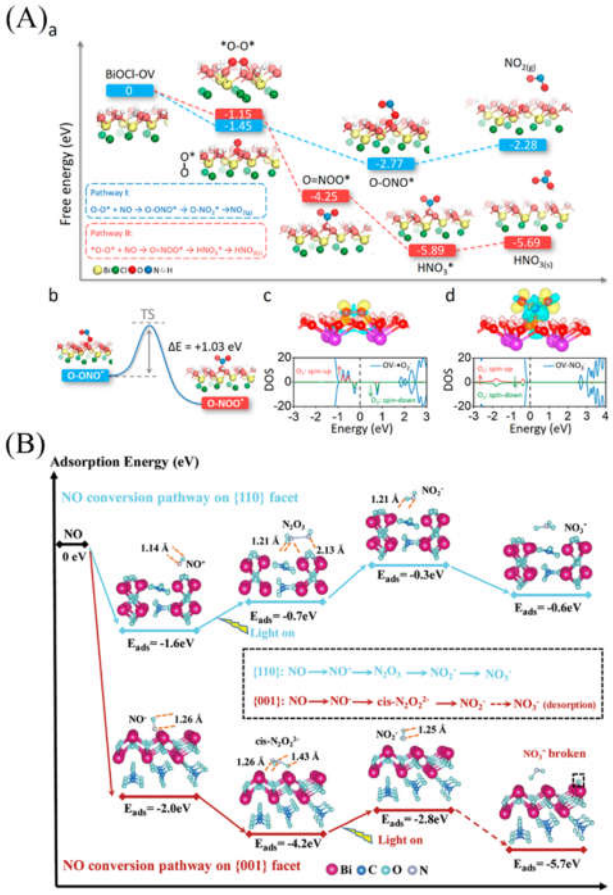

Figure 5. (**A**) Free energy change versus reaction coordinates for the oxidation of NO by $\bullet O_2^-$ on BiOCl(001) surface in different geometries. Reprinted with permission from reference [128]. (**B**) Adsorption energy and bond length of several major intermediate adsorption products on 110-BOC and 001-BOC. Reprinted with permission from reference [129].

6. Room Temperature Catalysis

Room temperature (or ambient temperature) catalysis is considered as one of the most energy-efficient methods because there is barely any energy requirement for heating, and this makes it another appealing technology for eliminating low levels of NO_x in semi-closed spaces, such as underground tunnels and for ppm levels of HCHO in new buildings [135]. Ambient temperature catalysis is a complete destruction/oxidation process that uses ROS, rather than liquid or AC adsorption, which need frequent replacement or regeneration. Two main advantages of room temperature catalysis are the energy savings and the absence of secondary pollution [136–138].

Indeed, considerable effort has been dedicated to the development of highly efficient and selective catalysts to achieve the complete degradation of HCHO and NO_x at room temperature. For HCHO removal, transition metal oxides, including cobalt oxides [139], manganese oxides [140–143], nickel oxides [144] and titanium oxides [145], and noble metal nanoparticle catalysts (i.e., Ag, Au, Pt, Rh and Pd) [146–150] are commonly used. For NO_x removal, transition metal oxides, especially cobalt and manganese oxides are often used [151]. Table 3 summarizes the types of catalysts commonly used for the oxidation of HCHO and NO_x under ambient conditions.

Table 3. Summary of typical catalysts for the removal of HCHO and NO_x at ambient conditions.

Catalyst	Pollutant	Temperature	Experimental Conditions	Catalytic Activity	Reference
MnO_x	HCHO	Room temperature	Fixed-bed reactor; (HCHO) = 30 ppb to 200 ppb; Catalyst: 0.11 g	80% conversion efficiency, 100% mineralization	[143]
MnO_2	HCHO	21 to 25 °C	Glass vessel (1.16 L); (HCHO) = 520 ppm; Catalyst: 0.5 g	94% of HCHO conversion into CO_2 at 21 °C	[152]
MnO_2 (α, β, γ and δ phase)	HCHO	50 to 200 °C	Fixed-bed reactor; (HCHO) = 170 ppm; 25% RH; Space velocity = 100,000 mL/g/h	100% HCHO conversion: δ-MnO_2 > α-MnO_2 > γ-MnO_2 > β-MnO_2 (80 °C, 125 °C, 150 °C and 200 °C)	[153]
Birnessite	HCHO	Room temperature	Glass bottle (3.5 L); (HCHO) = 200 ppm;	84.7% HCHO conversion over S-30 sample (dried at the temperature of 30 °C)	[141]
Ag/MnO_2	HCHO	20 to 120 °C	Fixed-bed reactor; (HCHO) = 500 ppm, 1300 ppm; GHSV [a] = 60,000 h^{-1}, 150,000 h^{-1}	8.9% Ag/MnO_2 shows a high normalised rate (10.1 $nmol \cdot s^{-1} \cdot m^{-2}$) and TOF = 0.007 s^{-1} at 110 °C under 1,300 ppm of HCHO and 150,000 h^{-1} of GHSV	[154]
1 wt % Pt (Rh, Pd and Au)/TiO_2	HCHO	20 to 120 °C	Fixed-bed flow reactor; (HCHO) = 100 ppm; GHSV = 50,000 h^{-1}, 100,000 h^{-1}, 200,000 h^{-1}	Pt/TiO_2 (100% HCHO conversion) > Rh/TiO_2 > Pd/TiO_2 = Au/TiO_2	[155]
0.78–0.98 wt % M/CeO_2 (M = Pt, Pd, Au and Ag)	HCHO	20 to 120 °C	Fixed-bed flow reactor; (HCHO) = 600 ppm; GHSV = 120,000 h^{-1}, 240,000 h^{-1}, 360,000 h^{-1}	~100% over Pd/CeO_2 at 20 °C	[156]
1 wt % Pt/Fe_2O_3	HCHO	25 to 100 °C	Fixed-bed reactor; (HCHO) = 100 ppm to 500 ppm; Catalyst: 0.2 g	100% HCHO conversion over Pt/Fe_2O_3-CD	[157]
Au/ZrO_2/PET	HCHO	Room temperature	Fixed-bed reactor; (HCHO) = 0.5 ppm, GHSV = 8000 h^{-1}	Close to 100% HCHO conversion	[158]
X-Mn bimetal oxides (X = Co, Ni, Zn)	NO	25 °C	Fixed-bed flow reactor; (NO) = 10 ppm; space velocity = 120,000 mL/g/h	100% NO removal in time duration up to 1.8 h over Co_1Mn_6-300 catalyst	[159]
Fe–Mn binary oxide	NO	25 °C	Fixed-bed flow reactor; (NO) = 10 ppm; GHSV = 40,000 h^{-1}	4 h for 100% NO removal over Fe_1Mn_4-300 sample	[160]
Mg-SC-OMS-2	NO	Room temperature	Fixed-bed flow reactor; (NO) = 10 ppm; space velocity = 120,000 mL/g/h	10% Mg-SC-OMS-2; 99% NO removal for 8 h in dry atmosphere; 96% NO removal for approximately 25 h (70% relative humidity)	[161]

Weak crystallization manganese oxide (WMO)	NO	25 °C	Fixed-bed flow reactor; (NO) = 10 ppm; GHSV = 40,000 h^{-1}	100% NO removal capability for approximately 20 h; >70 h for >80% NO removal (60% relative humidity)	[162]
Amorphous manganese oxides	NO	25 °C	Fixed-bed flow reactor; (NO) = 10 ppm; space velocity = 120,000 mL/g/h	10 and 21 h for 100% and 60% NO removal, respectively; 237 h for 90% NO removal (50–90% RH)	[163]
Active carbon	NO	Room temperature	(NO) = 380 ppm, space velocity = 6000 mL/g/h	~50% removal for 20 h	[164]
Zeolite	NO	30 °C	(NO) = 500 ppm, space velocity = 32,432 mL/g/h	~30% removal for 20 min	[165]
Chromic oxide	NO	30 °C	Fixed-bed flow reactor; (NO) = 15 ppm, space velocity y = 86,400 mL/g/h	>65% NO conversion for 500 min	[166]
CrO_x-ZrO_2	NO	25 °C	Fixed-bed flow reactor; (NO) = 12 ppm; space velocity = 45,000 mL/g/h	100% NO conversion for nearly 26 h over Cr_8Zr_1-300 catalyst	[167]
Cr-M mixed oxides (M=Co, Fe, Ni)	NO	25 °C	Fixed-bed flow reactor; (NO) = 12 ppm; space velocity = 45,000 mL/g/h	100% NO conversion for over 30 h on Cr_8Co_1-300 sample	[168]

[a] GHSV stands for gas hourly space velocity.

6.1. Key Variables Underpinning Catalytic Efficiency

6.1.1. Structure, Crystallinity, and Surface/Interface State

The catalytic performance of nanomaterials is largely dependent on their structural properties (i.e., particle size, surface area, pore structure and phase structure), electronic properties, and surface/interface state (i.e., O species and surface composition). The designs of the catalysts are determined by the reaction conditions for which they will be used and the methods used for their synthesis. For example, Zhang et al. compared the activities of α-, β-, γ- and δ-MnO_2 for HCHO removal at 80 °C and found that tunnel structure and active lattice oxygen species were mainly responsible for the excellent catalytic performance of δ-MnO_2 [153]. The tunnel structure of δ-MnO_2 is built by edge-sharing octahedral MnO_6 with water molecules and selected cations (e.g., Li^+, Na^+, K^+ and Ca^{2+}) located between layers to balance excess charge [141,169,170]. Chen et al. also reported that the tunnel structure of manganese oxides is the major influencing factor for catalytic HCHO removal [171].

Cryptomelane with 1D tunnels exhibit excellent catalytic activity that can be explained by tunnel cross sections of ca. 0.46 × 0.46 nm that were similar to the dynamic diameter of the HCHO molecule [171]. Besides, OVs produced as a result of the large fractions of Mn^{3+} ions in the MnO_2 framework served as active sites that promoted catalytic activity [172,173]. Bai et al. also reported that an increase in the quantities of Mn^{3+} ions over Ag/MnO_2 can promote the formation of OVs and in so doing facilitate catalytic activity [154]. Thus, regulation of surface OVs is an effective means of promoting catalytic HCHO removal.

Recently, our group synthesized tetragonal-monoclinic nano-zirconia (ZrO_2) phase junction nanomaterials (TMZ) (Figure 6a), which exhibited higher conversion rates for HCHO into CO_2 compared with pure ZrO_2. The enhanced catalytic property was attributed to the adsorption enhancement of Zr-rich sites and single electron activation at TMZ interfaces. Those effects cause C–H dissociation of HCHO and hydrogenation of O_2, thus lowering the activation barrier for HCHO oxidation [174]. Our group also reported that nitrogen-doped, carbon-encapsulated small Co nanoparticles (Co@NC) (Figure 6b,d) for HCHO oxidation at room temperature achieved >80% HCHO conversion efficiency [168]. Metallic Co nanoparticles were identified as the active sites for O_2 dissociation through density-functional theory (DFT) calculations [175].

In related work, Li et al. systematically synthesized MnO_x-CeO_2 to tailor the exposure of three major facets (Figure 6e), among which the MnO_x-CeO_2 with exposed (111) facets (MCO-111) showed higher activity for formaldehyde oxidation and CO_2 selectivity compared with two low-index (110) and (001) facets [176]. Furthermore, the oxygen vacancies were highly stable on the (111) facet, and the high migration rates for bulk lattice oxygen were able to replenish the surface lattice oxygen consumed, resulting in good activity and stability. The highly active regions exposed at the (111)-dominated surfaces were evident in IR thermography images, which also showed that Lewis acid−base properties of (111) surface facilitated oxygen mobility and activation.

For NO elimination at room temperature, several types of catalytic materials, such as metal oxide catalysts (Co_3O_4) [177] ,CrO_x-based [166–168] and MnO_x-based [159–163] catalysts), molecular sieves (Na-ZSM-5 [165]), and carbon nanofibers[164,178], have been studied thus far. The amorphous structures of these catalysts are critical for maintaining high activity and durability. For instance, Wang et al. [167,168] demonstrated that chromic-based amorphous oxide catalysts were active in ambient-temperature NO oxidation. These authors prepared a series of CrO_x-ZrO_2 mixed oxide materials with high surface areas and homogeneous amorphous phases, and those mixed oxides exhibited 100% conversion rates for low NO concentration at 25 °C over extremely long times (nearly 30 h). A similar conclusion was reached by Shi et al. who showed that mesoporous,

amorphous Mn-based oxides with low crystallinity and defects (OVs or Mn vacancies) were beneficial for high catalytic performance [159–163].

Nanostructured, Mg-doped manganese oxides (Mg-SC-OMS-2) showed low crystallinity with large surface areas and extensive defects, and they retained 99% NO removal efficiencies for as long as 8 h under an extremely high gas space velocity of 120,000 mL g^{-1} h^{-1}. The OVs in Mg-SC-OMS-2 improved the activity of the material for the additional activated O species generated via the Mars-van Krevelen (MvK) pathway [161]. In another study, the excellent performance of a nanoflower-like, weakly-crystallised manganese oxide was associated with Mn vacancies and hydrated surfaces, which can reduce the reaction barriers of the rate-determining steps [162]. Mesoporous X-Mn (X = Co, Ni, Zn) bimetallic oxides demonstrated substantially enhanced efficiencies in NO removal compared with their single-metal oxide (MnO_x, Co_3O_4, NiO and ZnO) counterparts [159].

As discussed above, the addition of ZrO_2 to stabilise the key Cr^{6+} redox sites can improve catalytic performance. In studies of Cr–Co, Cr–Fe and Cr–Ni oxide catalysts, the best performing catalyst achieved 100% NO conversion over ~30 h of operation at a high space velocity of 45,000 mL g^{-1} h^{-1} [168]. Finally, the presence of the surface hydroxyl groups on chromic-based oxide catalysts is equally important for high catalytic activity and long-term stability [166]. In summary, amorphous structures, OVs, and surface hydroxyl groups can enhance the catalytic oxidation of NO_x at ambient temperatures.

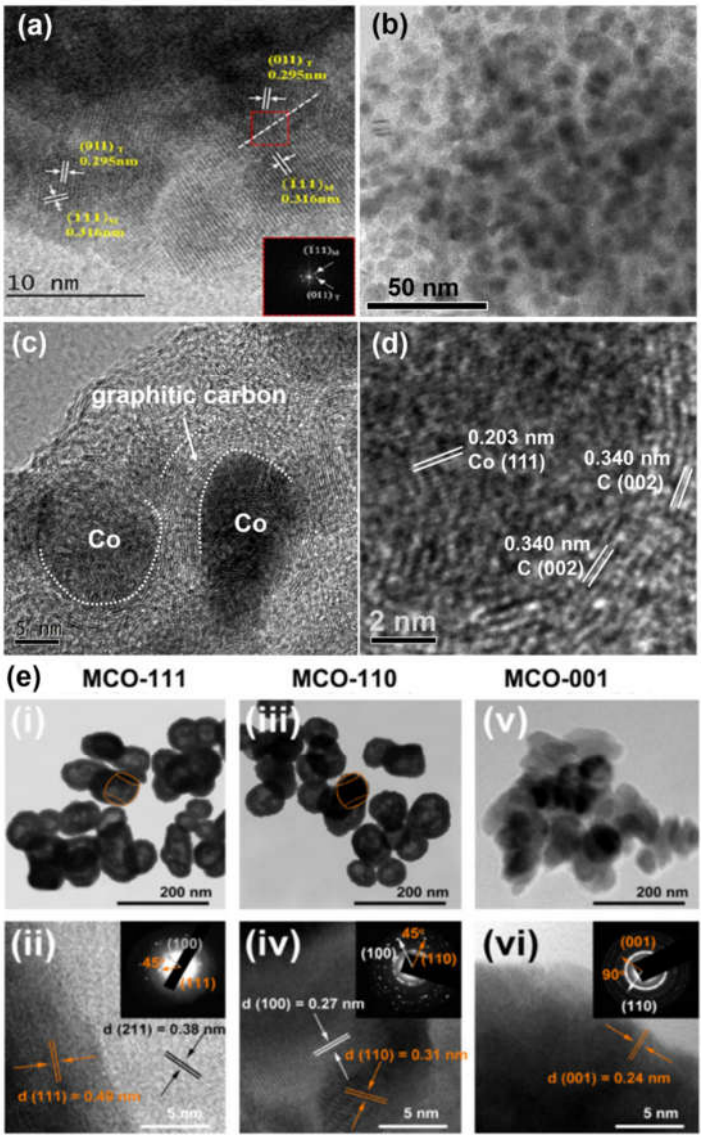

Figure 6. (**a**) High-resolution transmission electron microscopy (HRTEM) image of the TMZ-400 sample. Reprinted with permission from reference[174]; (**b**) TEM and HRTEM (**c**) images of Co@NC. Panel (**d**) is enlarged image of (**c**). Reprinted with permission from reference [175]. (**e**) TEM and HRTEM images of MCO catalysts with different exposed facets (**i** and **ii** correspond to TEM and HRTEM images of MCO-111 facet, respectively; **iii** and **iv** correspond to TEM and HRTEM images of MCO-110 facet, respectively; **v** and **vi** correspond to TEM and HRTEM images of MCO-001 facet, respectively). Reprinted with permission from reference [176].

6.1.2. Noble Metal Loading

The types of noble metals and the amounts that are loaded on the catalysts can significantly influence performance. Zhang et al. investigated the effects of noble metals (i.e., Au, Rh, Pd and Pt) on catalysis of HCHO [155,147], and they reported the following order of activity for the supported noble metal catalysts under the same reaction conditions (20 °C, 100 ppm HCHO, 20 vol% O_2, He balance, GHSV = 50,000 h^{-1}): Pt/TiO_2 >> Rh/TiO_2> Pd/TiO_2 = Au/TiO_2. The enhancement of catalytic activity was attributed to a 'strong metal-support interaction' (SMSI) effect. Amongst a variety of influencing factors, including size, morphology, and electronic state of the supported catalysts, the SMSI effect is an intrinsic factor that can increase catalytic activity [179]. That is, SMSI can stabilise the morphology of metals, lead to strong reactant adsorption, and facilitate activation [180].

The SMSI effects also include enhanced O_2 chemisorption, which promotes the oxidation of pollutant molecules [180]. More specifically, the SMSI between Au and CeO_2 can weaken Ce–O bonds, thereby generating OV, and as a consequence, gas-phase O_2 molecules are readily activated to promote HCHO oxidation [181].

In terms of theory, DFT calculations indicate that the SMSI can lead to perturbations of electronic properties of the catalysts, and in doing so, enhance electronic interactions between components [182]. Moreover, SMSI can also modulate the chemical states of Ir species and affect reaction selectivity in that way [183]. Given the promising results obtained thus far, the SMSIs between noble metals and metal oxides and their associated effects on gas adsorption and O_2 dissociation for HCHO and NO_x control should continue to be investigated.

6.1.3. Gas Hourly Space Velocity

In dynamic test systems of HCHO or NO_x catalytic oxidation, GHSV is a critical influence on catalytic performance because it directly affects the residence time of pollutants in the reactor or the contact time between pollutants and catalysts. Generally, the removal efficiency of HCHO or NO_x will decrease with increasing GHSV if other reaction conditions are held constant [156,184–186]. For instance, Huang et al. studied the HCHO removal efficiency over 0.1% Pt-TiO_2 catalyst under different GHSV conditions [184]. The results showed that complete removal (100%) of HCHO was achieved at the GHSV of 40,000 h^{-1} (at room temperature, 10 ppm HCHO concentration, 50% humidity), while the 99.1%, 97.8% and 90.5% removal efficiencies of HCHO were obtained at GHSVs of 80,000, 160,000 and 240,000 h^{-1}, respectively.

Liu et al. studied trends in HCHO conversion over Pt-TiO_2 for increases in GHSV from 5,000 h^{-1} to 250,000 h^{-1} (30 °C, 10 ppm HCHO inlet concentration), and that study showed that the HCHO conversion decreased at first, and gradually reached a plateau when GHSV increased to 80,000^{-1} [185]. That is because high GHSV reduces the residence time of HCHO molecules over catalysts. Li et al. found that the HCHO conversion efficiency significantly decreased from 98% to 37% when GHSV increased from 12,000 to 360,000 h^{-1}, especially at 20 °C over a Pd/CeO_2 catalyst [156]. For higher reaction temperatures, the decrease in HCHO conversion became less significant.

6.1.4. Relative Humidity

Similar to what happens in photocatalytic reactions, the presence of water vapor can also affect other types of catalysts at room temperature. For example, Chen et al. demonstrated that water vapor is beneficial for HCHO removal over supported gold catalysts [187,188]. Under a range of RH from 50%–75%, HCHO was completely oxidised to CO_2 and H_2O at room temperature (80 ppm HCHO, 34,000 h^{-1} GHSV). However, the conversion efficiency of HCHO decreased by more than 10% in the absence of water. An abundance of water vapor favours the production of surface hydroxyl groups which promote the conversion of HCHO to formate, an important intermediate that can be further oxidised to CO_2 and H_2O.

An overabundance of water, however, can induce the competitive adsorption of HCHO and H_2O on active sites, and that will impede HCHO removal. More specifically, Huang et al. compared the influence of RH on the removal efficiency of HCHO over 0.1% Pt/TiO_2, and the results showed the following decreasing trend in conversion efficiency: 25% ≈ 50% > 75% > 97.5% >> 0% (10 ppm HCHO, 25 °C and 80,000 h^{-1} GHSV) [184]. For NO oxidation, Shi et al. reported that water vapor enhanced catalytic stability over mesostructured, amorphous manganese oxides [172]. The maximum NO removal efficiency of 90% lasted over 237 h under a RH range of 50–90%, and the removal efficiency barely showed any effects of RH The stability was due to the formation of volatile HNO_3 molecules (i.e., $3NO_2 + H_2O = 2HNO_3 + NO$), which are easily carried away by that air flow, rather than forming NO_3^- that could block the active sites.

Similarly, Mg-SC-OMS-2 showed an increase in NO removal under high humidity at room temperature. On one hand, H_2O can help replenish O-containing species, but on the other, water vapor can impede NO_3^- deposition [161]. In another study, water vapor was found to inhibit NO removal on a Fe–Mn oxide catalyst, and the removal efficiency significantly decreased under 88% RH due to the competitive inhibition of the NO_x adsorption/absorption sites by water molecules [160]. The evidence summarized above indicates that there is an optimal RH range for each unique catalyst, and this should continue to be investigated.

6.2. Catalytic Conversion Mechanisms

Generally, three typical reaction mechanisms, namely, the (i) Langmuir–Hinshelwood (L–H), (ii) Eley–Rideal (E–R) and (iii) Mars-van-Krevelen (MvK) mechanisms are involved in the catalytic conversion of pollutants at room temperature. In the L–H mechanism, a two-stage redox process takes place as follows: (1) The catalyst surface is partially oxidised by O_2 from the gas phase to form surface O species—this is non-equilibrium dissociative adsorption of O and not the classical oxidation on a catalyst surface. (2) Then, surface O species react with the pollutants that are weakly pre-adsorbed on the surface, and in the meantime, the oxidised catalyst surface is reduced by pollutant molecules [189–191]. For the L–H mechanism, the controlling step is the surface reaction between two reactant molecules adsorbed on adjacent active sites. Different from the L–H mechanism, in the E–R mechanism, one reactant molecule from the gas phase reacts with another reactant molecule that was previously adsorbed on the catalyst surface. In the case of the MvK mechanism, the lattice oxygen on the catalyst surface participates in the reaction, and it can be supplemented by the oxygen obtained from the gas phase [149,192].

Catalytic oxidation is a highly complex process, and reactions of this type often are affected, if not controlled, by the behaviour of reaction intermediates [193]. Theoretical calculations can be used to predict reaction pathways and mechanisms, and that information can be used to better understand the process. For example, on the surface of Mn-doped, oxygen-defective CeO_2, HCHO can adsorb onto Ce–O bridge sites and O_2 onto adjacent O defect sites. Following that, HCHO is dehydrogenated to HCO–, and the dissociated H combines with O_2 to form –OOH. The HCO– continues to dehydrogenate to CO which then reacts with O from the dissociation of –OOH to form CO_2 and H_2O [194].

The process just described is an example of the L–H mechanism. Metal oxides with alterable cation oxidation states can serve as active sites that trigger HCHO oxidation, which is under control of the MvK mechanism [181,149,195]. Specifically, on Au/CeO_2 surfaces, HCHO captures a lattice oxygen and forms HCOOH; this is followed by O_2 occupying the oxygen defect site. The O_2 later dissociates and reacts with HCOOH to form H_2CO_3, which in turn further dissociates into CO_2 and H_2O [181]. For $Pt\text{-}Bi_2WO_6$ nanosheet catalysts, HCHO is first adsorbed through H bonding with a surface hydroxide radical. The HCHO captures one lattice oxygen and forms CH_2O_2 (dioxymethylene, DOM) with one remaining oxygen defect. Subsequently, the DOM undergoes isomerization and transforms into HCOOH. The O_2 adsorption and steps that follow are similar to what occurs on Au/CeO_2 surfaces [195]. For HCHO oxidation on $K\text{-}Ag/Co_3O_4$ surfaces, HCHO is first dehydrogenated to HCO–, and that is followed by the acquisition of one lattice oxygen to form CHOO and a OV site which can be repaired by O_2 adsorption. Finally, CO_2 and H_2O are formed through metal cation centred re-oxidation [149].

Surface OVs can promote the activation of oxygen molecules and the replenishment of ROS. As shown in Figure 7a, on Co_3O_4 catalysts with surface OVs, the transfer of active oxygen can be significantly facilitated by a synergistic effect between Co^{3+}/Co^{2+} and O/Vo redox. Once HCHO molecules adsorb onto the surface, they can be readily oxidized into formate species and eventually converted into CO_2 and H_2O by reacting with ROS [196]. For ferrihydrite (Fh) supported Pt catalysts (Pt/Fh) (Figure 7b), HCHO and O_2 were first simultaneously adsorbed onto the Fh and Pt surfaces, respectively; wherein the abundant

surface hydroxyl groups on Fh were beneficial to HCHO adsorption via hydrogen bonding between an oxygen atom of HCHO and a hydrogen atom of the surface -OH. Then, the active oxygen radicals generated through O_2 splitting attacked the carbon atom of HCHO to from DOM intermediates, which further transformed into formate by the addition of an active surface oxygen atom. The adsorbed formate was subsequently oxidized into adsorbed CO_2 (CO_{2ads}) and H_2O (H_2O_{ads}) by an active hydroxyl radical and finally desorbed from the Pt surface [197].

By combining the results of in situ DRIFTS and DFT calculations, our group proposed a MvK reaction pathway for HCHO oxidation over cobalt nanoparticles encapsulated in porous nitrogen-doped carbon (Co@NC) (Figure 7c). As proposed, HCHO and O_2 molecules initially adsorb onto Co@NC. Then, the adsorbed O_2 on the Co^0 surface dissociates into active oxygen radicals, oxidizing the adjacent HCHO to formate species, which are further oxidized to adsorbed CO_2 and H_2O that ultimately desorb from the Co surface [175].

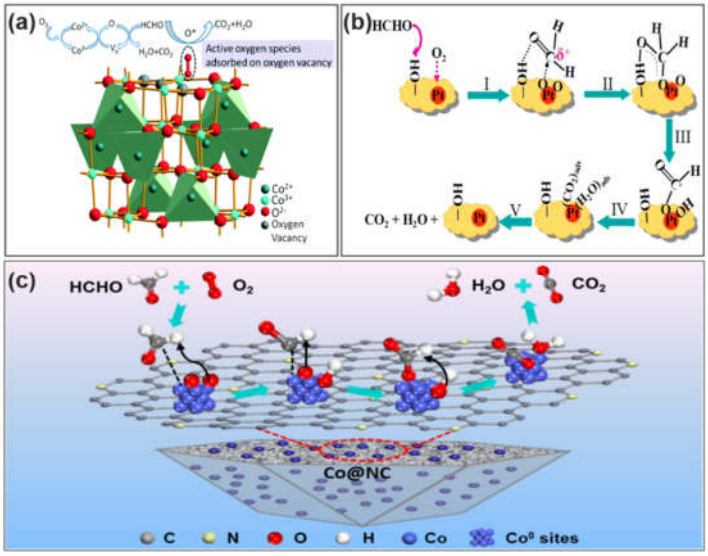

Figure 7. (**a**) Reaction mechanism of HCHO oxidation over Co_3O_4 with surface oxygen vacancies. Reprinted with permission from reference [196]. (**b**) Reaction pathway for complete oxidation of HCHO over the Pt/Fh. Reprinted with permission from reference [197]. (**c**) Schematic illustration and reaction pathway of catalytic-oxidation of HCHO on the Co@NC catalyst at room temperature. Reprinted with permission from reference [175].

Various mechanisms for NO catalytic oxidation over other catalysts also have been uncovered; for instance, Cr_2O_3 with exposed (001) surfaces tends to follow the E-R mechanism, in which NO in the gas phase directly reacts with adsorbed O_2 to form NO_2. This accounts for the strong adsorption of O_2 onto unsaturated Cr3c sites [142,198]. For Mg-doped manganese oxide surfaces, the NO catalytic oxidation process follows the typical MvK mechanism. That is, the lattice oxygen is consumed by reaction with NO, and this is accompanied by the reduction of Mn^{4+} to Mn^{3+}. Subsequently, Mn^{3+} is reoxidized to Mn^{4+} through oxygen replenishment to close the redox cycle [161]. A similar mechanism has been observed for amorphous CrO_x-ZrO_2 catalysts [167].

Ideal catalysts for industrial applications would be efficient, selective, and durable. In practice, however, the accumulation of intermediate hetero atoms that can cause poisoning by halogens or sulfur leads to incomplete oxidation. Moreover, the growth of catalyst particles inevitably leads to catalyst deactivation [139,142,190,199,200]. In essence, because the MvK mechanism is a redox reaction, [201] strong interactions between the catalysts and surface-active species can hinder continuous redox cycling, and this can also cause catalyst deactivation [167,201,202].

7. Applications of Ambient Air Purification by Nanotechnologies (APN)

7.1. Catalyst Immobilization

Functional nanomaterials are essentially solid powders, and therefore, immobilization on support materials or films is necessary for practical applications, otherwise it would cause severe pressure drops or mass loss [136]. The choice of an appropriate support for immobilizing photocatalysts is based on several considerations as follows: (I) photocatalytic activity should not be inhibited after the immobilization process. For example, a structured ceramic foam was used to immobilize a *g*-C_3N_4 photocatalyst, and its photocatalytic performance was not degraded but enhanced [203]. (II) catalyst powders must possess good adhesion properties for the support material because any released nanomaterials could pose threats to human health [204]. (III) the support material should have a large specific surface area and be chemically inert; and (IV) the support material should be mainly composed of raw materials and inexpensive. In addition to ceramic foams, other types of substrates such as optical fibres [205], porous lava [206], fiberglass [207], quartz [208], glass [209], and stainless steel [210] are often used for immobilization. Glass substrates are extensively utilised because of their good light transmittance and ease of cleaning [211].

Sol-gel synthesis [212], dip coating [213], chemical or physical vapor deposition [214], and electrophoretic methods [215] have been used to immobilise photocatalysts on various supports. Of these, the sol-gel method, which exhibits high versatility, has been widely adopted for depositing different precursors, such as titanium alkoxide, titanium tetrachloride or titanium halogenide, on substrates [216]. Recently, Huang et al. fabricated protonated g-C_3N_4/Ti^{3+} self-doped TiO_2 nanocomposite films (p-CN/TiO_2) on glass substrates, and that appears to be an effective new approach for making photocatalysts adhere to a substrate at room temperature [217]. For room temperature catalyst immobilization without the need for light penetration, honeycomb ceramics [218], cellulose fibres [219], and AC [220,221], are common solid supports. Of these, AC exhibits superior mass transfer due to its high surface area and high porosity [222].

Liu et al. investigated the mechanism for NO oxidation over Na-ZSM-5 molecular sieves with high SiO_2/Al_2O_3 ratios [165]. The results showed that the NO catalytic oxidation process was accompanied by a significant adsorption of NO_2, thereby causing a dynamic equilibrium between NO_2 adsorption and NO oxidation. In another study, Wang et al. found > 60% NO removal at room temperature on porous carbon nanofibers (PCNFs) for an inlet NO concentration of 20 ppm [178]. The removal mechanisms included NO adsorption, catalytic oxidation to NO_2, and partial reduction to N_2 by PCNFs due to the large surface area and abundance of N species. The development of air purification technologies based on functional nanomaterials does present significant practical challenges, but there is a good potential for achieving the final objectives.

7.2. Passive Systems for APN

7.2.1. Roadside

Air pollution due to excessive NO_x emissions is a major issue near roads where traffic is heavy and in tunnels and underground parking lots, and this is a special concern for people who spend a significant amount of time in those places. To address the problem, TiO_2 photocatalysts have been combined in novel ways with cement for pavements or coverings on clays and other construction materials to eliminate NO_x in urban environments since the end of 1980s [223–225]. This process is regarded as a passive air purification strategy because natural sunlight is used to activate the photocatalytic material, and pollutant molecules freely diffuse onto the surface,with examples shown in Figure 8. Laboratory studies by Bianchi et al. [226] were conducted to evaluate the deNO_x performance of full-sized industrial photocatalytic porcelain tiles. Under realistic gas flow rates and NO_x concentrations (100 ppb) conditions, the NO_x conversion in July was found

to be higher than that in September, and that was explained by the difference in light irradiance.

Although reasonable photocatalytic performance of these engineered construction materials has been achieved in the laboratory, field studies have shown mixed results. For example, Maggos et al. found that a decrease in NO_x concentration levels in an indoor car park where TiO_2 paint had been applied was significant, whereas Gallus found no photocatalytic beneficial effect on NO_x, O_3, or VOCs in an artificial street canyon in Italy compared with a reference site [227–229]. In another full-scale experiment supported by the EU, TiO_2 containing concrete pavement on a street in Hengelo, The Netherlands showed a maximum of 45% NO_x removal efficiency under ideal weather conditions [230]. A positive result was also obtained in field studies in Copenhagen where NO abatement reached a peak higher than 45% at the summer solstice [231]. Our recent field study suggested even higher deNO_x performance was achieved over g-C_3N_4/TiO_2 composite pavements during rush hour, indicating the diffusion and adsorption of low level NO_x in open space are equally crucial [232]. The discrepancies in air cleaning effects of these engineered materials were likely caused by differences in the photocatalytically active surface area-to-volume ratios (S_{active}/V) at the field sites, but other factors can also help explain the differences.

For instance, daytime and nighttime studies should be conducted to provide an integrated value for reduction efficiency in urban environments. Sampling height is another important factor that can influence the remediation results because sampling few centimetres away from the active photocatalyst surface results in a much higher NO_x reduction value compared with sampling at a height of 3 m, which is typical of an urban network monitoring station. Variations in pollutant emissions and dispersion can affect transport to the active surface, and that can affect the remediation results [229]. Although the results have not always been positive, this innovative technology deserves continued research because it may be suitable for the treatment of low concentrations of pollutants (sub-ppm level), and it has low implementation and operating costs compared with other techniques.

7.2.2. Indoor Environment

There are many sources for formaldehyde, toluene, and various other VOC species, and NO_x, in household environments; these include combustion sources, especially emissions from cooking; outgassing from interior furnishings and paints; and the infiltration of polluted outdoor air. Indoor air pollution has become a serous concern because pollutant concentrations can be high and exposures long—indeed, humans spend > 80% of their time indoors and that increase the risk of harmful effects. Early in 1995, the U.S. Environmental Protect Agency started investigations into the photocatalytic oxidation of indoor VOCs, including formaldehyde, benzene and polycyclic aromatic hydrocarbons (PAHs).

Indoor environments have conditions that are different from the outdoors, such as low air flows (<1 L min^{-1}) and low visible light intensities, and only nontoxic photocatalytic materials are suitable for indoor use [233]. Taking these constraints into consideration, Lorencika et al. developed a water-based photocatalytic coating (C-TiO_2) on wallpaper that had made use of visible light, and that material showed 18% deNO_x performance for an initial NO_x concentration of 500 ppb. These researchers suggested that the pretreatment method they used to expose the active component was directly related to the deNO_x effectiveness. Indoor lighting optimization also would be a way to enhance photocatalytic efficiency. Gandolfo et al. [234] studied the effectiveness of TiO_2-embedded photocatalytic wall paints on NO_2 conversion in an indoor environment, and HONO, a potentially harmful intermediate, was found to be formed while NO_2 was being destroyed. This shows that thorough evaluations of potential problems with APN methods, especially the generation of secondary pollutants, need to be conducted in addition to the more straightforward assessments of the efficacy of NO removal.

7.2.3. Tunnels and Indoor Parking Lots

Conditions unfavourable for pollutant dispersion cause city tunnels and indoor parking lots to be among the most polluted places, often with high levels of NO_x, VOCs, and PAHs generated by vehicles, especially during rush hours and when large numbers of vehicles are starting their engines [235]. In 2012, a city tunnel in Rome was renovated with photocatalytic, cement-based paint on interior and exterior walls and a new lighting system [236]. In two successive environmental monitoring campaigns of 30 working days each, the NO_x abatement values were found to be an improvement of over 20% compared with a non-renovated tunnel. The best reduction value was observed in the centre of the tunnel, where the light intensity and wind speed were almost constant.

In 2015, another city tunnel renovation program was conducted in the Leopold II tunnel in Brussels, Belgium by researchers from five European countries. That study was funded as the Demonstration of Photocatalytic Remediation Processes on Air Quality Project, [228,230] and it showed a different effect compared with the study in Rome. In the heavily polluted Belgian tunnel, the photocatalytic surfaces were deactivated by dust and soot, there was low light irradiance, and wind speeds were high. Those conditions led to poor photocatalytic activity and unexpectedly low NO_x removal. Although the final results were disappointing, that study showed that high light intensity, low wind speeds, large active surfaces, and superior photocatalytic activity are required for successful remediation. In 2007, the EU sponsored a projected called the Photocatalytic Innovative Coverings Application for Depollution Assessment in which a photocatalytic coating was used to treat air pollution in an indoor parking lot. Results of that study, conducted by Maggos et al. [237] showed that the deNO_x ability of TiO_2-containing paint was ~20%, which was lower than that obtained in the laboratory, and that relatively low value was thought to be because organic compounds had interfered with NO_x oxidation in the parking lot.

The literature summary presented above shows that passive APN systems can be simple, cost-effective solutions for combating air pollution in some applications. However, the performance of these systems can be compromised in heavily polluted areas and in places with low light intensity and variable weather conditions. The rapid deactivation of photocatalysts and the generation of secondary pollutants are primary concerns relative to this technology.

7.3. Active Systems for APN

As discussed above, passive APN systems have significant limitations for effective pollutant abatement and their durability is an issue, and therefore, active APN systems have been introduced. These active systems typically incorporate light sources and blowers, and they often are combined with other techniques, such as filtration or adsorption (examples shown in Figure 8). In the discussion that follows, these systems are categorised based on their applications.

7.3.1. Air Cleaners for Indoor Environment

The efficiencies of passive APN systems can be severely restricted by insufficient mass transport and residence time of pollutants on the photocatalyst surface that were not ideal. These problems can be countered by installing a blower or a fan in the system to force air to flow over the photocatalyst surface. A typical example of an active APN apparatus is an indoor air cleaner. Conventional air cleaners use filtration to remove particle matter from the air, but they are generally ineffective for gaseous pollutants. Incorporating filtration with nanomaterial-based catalysis is a way to improve the performance of air cleaning units and increase the durability of the catalysts.

For example, Ao et al. [238] reported that an air cleaner with active carbon and HEPA filters had an extremely low capacity for NO removal. The addition of a TiO_2 filter to that system, however, resulted in the removal of almost 90% of the initial NO in 120 min under

irradiation with a UVC lamp. The use of a combined TiO_2/active carbon filter showed a further enhancement in NO removal, and what is more, the release of NO_2 was inhibited due to its adsorption onto the active carbon. Indeed, the adsorption of the gaseous contaminants on active carbon has two benefits (1) to increase the residence time of the pollutants under high flow rates and (2) to regenerate the adsorbent [56]. These studies demonstrate the advantages of combining filtration, adsorption, and photocatalysis for indoor air purification systems.

In addition to efficient mass transport, strong and uniform irradiance for air purifying devices is critically important for ensuring a high level of performance and suppressing the generation of undesirable intermediates. For example, Denny et al. [239,240] found that during the photodegradation of ethanol, the use of two blacklight blue (BLB) lamps with high irradiance reduced the production of acetaldehyde, a toxic intermediate. After replacing the BLB lamp with a UV-LED lamp, the peak concentration of acetaldehyde decreased by more than 10-fold due to the more uniform irradiation of the LEDs on the photocatalyst surface.

Slimen and Fujishima developed an indoor air purifier that used a TiO_2-impregnated Ti mesh filter as a cleaning unit, and it was found to be effective in decomposing cigarette smoke [241]. Weon et al. [69] developed a (001) facet-dominated TiO_2 nanotube photocatalyst filter, which showed improved activity for toluene, acetaldehyde, and formaldehyde removal compared with (101) facet exposed TiO_2 nanotubes (TNTs). These researchers further evaluated the removal of VOCs by a commercial air cleaner equipped with a (001)-TNT filter, and they found that it exhibited an average removal efficiency of 72% within 0.5 h; this level of performance met the Korean air cleaner standards protocol [69]. Feng et al. combined a triboelectric nanogenerator (TENG) with a photocatalysis technique to develop a self-powered electrostatic filter for formaldehyde removal [33].

7.3.2. Tunnel

The largest tunnel air cleaning system in central Hong Kong presently in use consists of eight units with advanced air cleaning equipment to cleanse the air for a nearby green space and commercial centre. Each cleaning unit is composed of an electrostatic dust collector, which is used to remove suspended particulate matter, and a special unit for NO_2 emitted from motor vehicles. A total of 5,400,000 m^3 of air in the tunnel can be treated each hour, and the removal efficiency of PM_{10} and NO_2 can be as high as 80% (http://www.3hk.cn/hk/2019/01/21/119325.html (Jan.21st, 2019), in Chinese).

7.3.3. Photocatalytic Solar Tower for an Industrial Zone

In Japan, small, unregulated industrial establishments emit low concentrations VOCs, which can lead to local air pollution. To control this problem, researchers devised a unique tower-like photoreactor that photodecomposes VOCs and is suitable for installation in confined spaces [242]. A cylindrical mirror with gratings was used to focus solar irradiation onto the interior of a reactor. A TiO_2-coated ceramic tube in the reactor effectively eliminated toluene vapor at 5 ppm, and its performance was almost solely dependent on solar intensity. Long-term monitoring for six months showed almost no decrease in photocatalytic activity, which suggests that the solar tower is suitable for the long-term remediation of atmospheric VOCs.

7.3.4. Catalytic Street Lamps

Recently, our group developed an enhanced outdoor air cleaning device for the elimination of PM and NO_x that combines filtration and photocatalysis with lighting. Practical considerations for structural design, key parameter optimization, and performance in real environments were taken into account during the development of these units. For these devices, pre-treatment with a filtration unit is used to remove particles, and a photocatalysis unit is used for further purification. The performance of the

device was evaluated through mathematical modelling and monitoring in a field deployment. The average elimination rates of NO were over 55% and 40% on sunny and rainy days, respectively, and the average filtration efficiency of $PM_{2.5}$ reached 70–80%. The overall purification efficiencies for $PM_{2.5}$, PM_{10} and NO_x for 200 devices installed in the Xi'an International Horticultural Expo Park were 4.3%, 9.0% and 16.1%, respectively, during a long-term deployment. Plans are being made to install enhanced outdoor air cleaning devices in large areas in the near future to improve air quality.

7.3.5. Hybrid Solar-Assisted Large-Scale Cleaning System (HSALSCS) for Large-Scale Air Cleaning

At present, active APN systems are most often used for indoor environments and relatively small spaces. Last year, Nature News reported on a prototype HSALSCS developed by Chinese and American scientists to combat urban smog in Xi'an, a provincial capital in central China [243]. The design and development of the HSALSCS have been discussed in detail by J. Cao elsewhere [244]. Briefly, a 60 m-high concrete chimney was built on top of a large glass solar collector, within which electric-powered blowers move the air through a series of filter banks. Particles are separated by the filter banks, and clean air billows from the top of the chimney.

Q. Cao et al. [245] from the aerosol group at the University of Minnesota ran a transient 3-D numerical model of fluid and heat flow for the system and validated the model with field measurements in January 2017. The analysis showed that the system's cleaning performance was largely dependent on physical parameters and factors, especially the amount of solar irradiation, solar collector width, and tower width and height. The pressure drop of the filters also was critically important. If the pressure drop becomes extremely high, additional fans (or blowers) must be used to strengthen the flow field [246].

During a one month field monitoring period, a 19% decrease in $PM_{2.5}$ concentration within a 10 km area was registered in air monitors surrounding the HSALSCS compared with monitors in other parts of the city. This study received strong positive feedbacks from world-renowned atmospheric scientists and chemical engineers who noted that this prototype provides an innovative approach for combating the public health hazard of urban smog. The HSALSCS was selected as one of "28 Incredible 'Made in China' Innovations that are Changing the World" in February 2019 (28 incredible 'Made in China' innovations that are changing the world (msn.com), 28 June 2019.

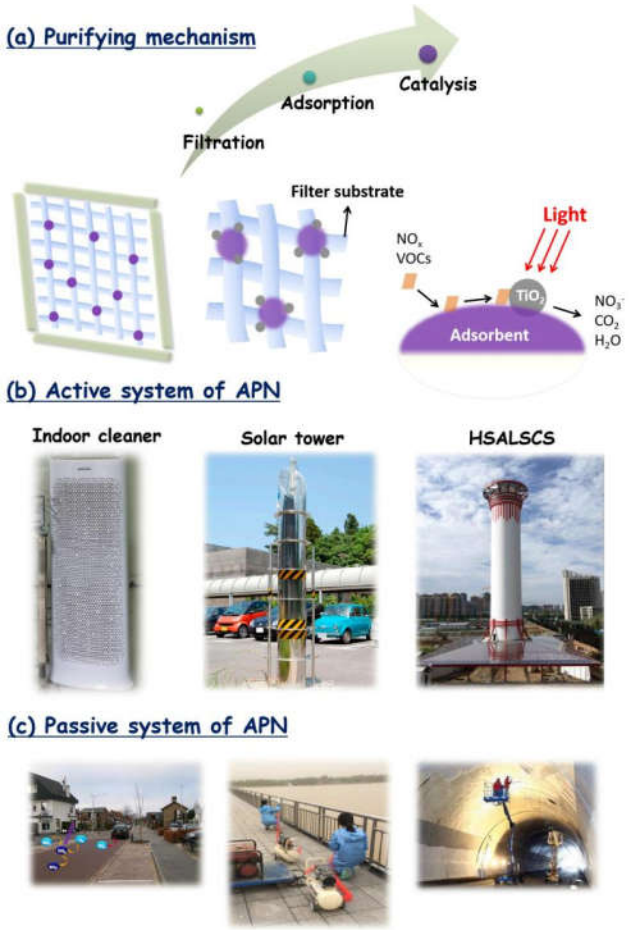

Figure 8. (**a**) The mechanism of active APN systems; (**b**) prototype cleaning systems at different scales. Reprinted with permission from reference [238,242,243] and (**c**) passive system of APN with TiO_2 embedded concrete pavements applied on roads, bridges, and tunnels. Reprinted with permission from reference [236,230].

In summary, the studies on the photocatalytic removal of air pollutants with nanomaterials have shown promising results, but their performance has varied with the specifics of the applications. Indeed, enhancements to catalytic activity will require the design more effective nanomaterials, and that in turn, will depend on a better understanding of the underlying mechanisms involved in the interactions between the nanomaterial surface/interfaces and pollutant molecules.

8. Conclusions and Future Perspectives

APN is a novel technology for combating air pollution that is characterized by low energy consumption and high efficiency. This review provides a general background on air pollution in China and highlights the need for developing ambient air control technology as a supplement to source control methods. Next, the most pressing and critical issues are considered; these include filtration, adsorption, and mild catalysis (photocatalysis and ambient temperature catalysis), including nanomaterial design and optimization, key environmental conditions, nanomaterial deactivation and regeneration. Finally, applications of photocatalytic air cleaning, and cleaning devices integrated with adsorption, filtration, or catalytic degradation technologies are discussed.

Although promising achievements in air pollution control technologies already have been made, future research is urgently needed to directly address the following issues:

1. The continued development of novel nanomaterials that feature strong visible light (up to 700 nm) absorption, fast charge transport, and low e^-/h^+ recombination is still desirable, especially for practical air pollution abatement applications.

2. Replacement of noble metals and rare metals in catalysts with more abundant materials, including non-metallic substances, such as metal-free *g*-C_3N_4 photocatalysts, carbon, perovskite, or other natural clay nanomaterials with high adsorption properties. This will benefit large-scale production and broaden applications.

3. Understanding the mechanism involved in interfacial charge transfer and ROS formation; the key factors governing reaction pathways and material deactivation deserve special attention.

4. Design of new APN devices to target pollutants in a range of micro-environments, and in combination with other cleaning devices, to combat street and even urban-scale air pollution.

5. With the outbreak of novel coronavirus disease (COVID-19) and the serious threat to public health that it poses, research opportunities are now emerging for investigations into the disinfection of airborne pathogens with nanomaterials. The formation of by-products by nanomaterials is minimal, and this adds to their attractiveness compared with traditional disinfectants such as O_3, H_2O_2, ClO_2, or UV irradiation [247]. Recently, some nanomaterials have been shown to provide broad-spectrum disinfectant properties; these include nanosilver (nAg), TiO_2 and carbon-based nanostructures [248–251].

The mechanisms that provide disinfection are another area of active investigation. For example, released silver ions (Ag^+) with high redox potentials can strongly bind to thiol groups (-SH) of viral or bacterial proteins, and this is thought to cause the denaturation of DNA molecules and lead to permanent disinfection and broad spectrum antimicrobial effects [247]. Disinfection from TiO_2 is due to the production of ROS through exposure to light—those substances disrupt the respiratory chains of bacteria and cause oxidative damage to cell membranes and nucleic acids. Nano-TiO_2 photocatalytic deactivation is effective for Gram-positive and Gram-negative bacteria and viruses [248,249]. The antimicrobial effects of CNT are different from nAg or TiO_2 because the damage caused by the tubes results from the physical puncturing of cell membranes [247]. Finally, the antimicrobial mechanism for the graphene family of materials has been reported to involve oxidative damage caused by ROS.

Optimization of the oxidation state, size, shape, and electronic structure of nanomaterials and surface functionality is a way to enhance antimicrobial activity. Overall, the deactivation mechanisms for viruses/bacteria can be quite variable among nanomaterials, and improvements in their effectiveness will require further research on material optimization and long-term stability, and verification of the mechanisms also will be needed. There are, however, some indications that the attachment of antimicrobial nanomaterials onto support polymers is a critical step toward practical air disinfection, and this is another area that deserves further investigation.

A literature survey has shown that Japan, Hong Kong, the United States and European Union countries have conducted a considerable number of trials in which nanomaterial-based catalysts were used for outdoor and indoor air purification. In comparison, China has made fewer attempts along these lines, and the results of only a few studies have been published. Therefore, efforts should be made in China to develop new, cost efficient, and functional air cleansing nanomaterials and to employ them in ways that benefit our society. Given the continued problems of air pollution and the growing numbers of pollutants expected in the future, APN technology can become more efficient and practical through focused research, and we believe it will pay large dividends in the mediation of air pollution throughout the world.

Author Contributions: Conceptualization, J.-j.C. and Y.H.; formal analysis, Q.Z. and Y.H.; writing—original draft preparation, Q.Z.; writing—review and editing, J.-j.C.; project administration, J.-j.C.;

funding acquisition, J.-j.C. All authors have read and agreed to the published version of the manuscript.

Funding: This research was funded by the Strategic Priority Research Program of Chinese Academy of Sciences, grant number XDA23010300 and XDA23010301; the National Key Research and Development Program of China, grant number 2017YFC0212200 and 2016YFA0203000, and the Youth Innovation Promotion Association of Chinese Academy of Sciences, grant number 2021413.

Acknowledgments: We acknowledge the support from the National Key Research and Development Program of China (grant No. 2017YFC0212200), the key program and the "Strategic Priority Research Program" of the Chinese Academy of Sciences (grant No. XDA23010300), the National Key Research and Development Program of China (grant No. 2016YFA0203000), and the Youth Innovation Promotion Association, grant number 2021413.

Conflicts of Interest: The authors declare no conflict of interest.

Abbreviations and Explanations

Abbreviation	Explanation
$PM_{2.5}$	Particulate matter of less than 2.5 μm in size
VOCs	volatile organic compounds
SOA	secondary inorganic aerosol
LNBs	low NO_x burners
MEIC	multi-resolution emission inventory for China
BTEX	benzene, toluene, ethylbenzene and xylene
SCR	Selective catalytic reduction
SNCR	selective non-catalytic reduction
TWC	three-way catalysis
APN	ambient air purification by nanotechnologies
TENG	triboelectric nanogenerator
AC	activated carbon
AOPs	advanced oxidation processes
ROS	reactive oxygen species
VB/CB	valence/conduction band
UV	ultraviolet
SPR	surface plasmon resonance
CDs	carbon nanodots
OVs	oxygen vacancies
RH	relative humidity
GC-MS	gas chromatography-mass spectrometry
in situ DRIFTS	In situ diffuse reflectance infrared fourier transform spectroscopy
SMSI	strong metal-support interaction
GHSV	gas hourly space velocity
L-H	Langmuir-Hinshelwood
E-R	Eley-Rideal
MvK	Mars-van-Krevelen
HSALSCS	hybrid solar-assisted large-scale cleaning system

References

1. Wang, L. The battle against $PM_{2.5}$ is on. *Natl. Sci. Rev.* **2014**, *1*, 315–317, https://doi.org/10.1093/nsr/nwu016.
2. Pui, D.Y.; Chen, S.-C.; Zuo, Z. $PM_{2.5}$ in China: Measurements, sources, visibility and health effects, and mitigation. *Particuology* **2014**, *13*, 1–26, https://doi.org/10.1016/j.partic.2013.11.001.
3. Cohen, A.J.; Brauer, M.; Burnett, R.; Anderson, H.R.; Frostad, J.; Estep, K.; Balakrishnan, K.; Brunekreef, B.; Dandona, L.; Dandona, R.; et al. Estimates and 25-year trends of the global burden of disease attributable to ambient air pollution: An analysis of data from the Global Burden of Diseases Study 2015. *Lancet* **2017**, *389*, 1907–1918, https://doi.org/10.1016/s0140-6736(17)30505-6.

4. An, Z.; Huang, R.-J.; Zhang, R.; Tie, X.; Li, G.; Cao, J.; Zhou, W.; Shi, Z.; Han, Y.; Gu, Z.; et al. Severe haze in northern China: A synergy of anthropogenic emissions and atmospheric processes. *Proc. Natl. Acad. Sci. USA* **2019**, *116*, 8657–8666, https://doi.org/10.1073/pnas.1900125116.
5. Huang, R.-J.; Zhang, Y.; Bozzetti, C.; Ho, K.F.; Cao, J.-J.; Han, Y.; Daellenbach, K.R.; Slowik, J.G.; Platt, S.; Canonaco, F.; et al. High secondary aerosol contribution to particulate pollution during haze events in China. *Nature* **2014**, *514*, 218–222, https://doi.org/10.1038/nature13774.
6. Guo, S.; Hu, M.; Zamora, M.L.; Peng, J.; Shang, D.; Zheng, J.; Du, Z.; Wu, Z.; Shao, M.; Zeng, L.; et al. Elucidat-ing severe urban haze formation in China. *Proc. Natl. Acad. Sci. USA* **2014**, *111*, 17373–17378.
7. Alvarez, E.G.; Wortham, H.; Strekowski, R.; Zetzsch, C.; Gligorovski, S. Atmospheric Photosensitized Heterogeneous and Multiphase Reactions: From Outdoors to Indoors. *Environ. Sci. Technol.* **2012**, *46*, 1955–1963, https://doi.org/10.1021/es2019675.
8. *WHO Guidelines for Indoor Air Quality: Selected Pollutants*; World Health Organization: Geneva, Switzerland, 2010.
9. Wang, S.; Ang, H.; Tade, M.O. Volatile organic compounds in indoor environment and photocatalytic oxidation: State of the art. *Environ. Int.* **2007**, *33*, 694–705, https://doi.org/10.1016/j.envint.2007.02.011.
10. Mamaghani, A.H.; Haghighat, F.; Lee, C.-S. Photocatalytic oxidation technology for indoor environment air purification: The state-of-the-art. *Appl. Catal. B Environ.* **2017**, *203*, 247–269, https://doi.org/10.1016/j.apcatb.2016.10.037.
11. Gómez-García, M.A.; Pitchon, V.; Kiennemann, A. Pollution by nitrogen oxides: An approach to NOx abatement by using sorbing catalytic materials. *Environ. Int.* **2005**, *31*, 445–467, https://doi.org/10.1016/j.envint.2004.09.006.
12. Skalska, K.; Miller, J.S.; Ledakowicz, S. Trends in NOx abatement: A review. *Sci. Total Environ.* **2010**, *408*, 3976–3989, https://doi.org/10.1016/j.scitotenv.2010.06.001.
13. Perring, A.; Pusede, S.; Cohen, R.C. An Observational Perspective on the Atmospheric Impacts of Alkyl and Multifunctional Nitrates on Ozone and Secondary Organic Aerosol. *Chem. Rev.* **2013**, *113*, 5848–5870, https://doi.org/10.1021/cr300520x.
14. Li, M.; Liu, H.; Geng, G.; Hong, C.; Liu, F.; Song, Y.; Tong, D.; Zheng, B.; Cui, H.; Man, H.; et al. Anthropogenic emission inventories in China: A review. *Natl. Sci. Rev.* **2018**, *5*, 603–603.
15. Kurtenbach, R.; Becker, K.; Gomes, J.; Kleffmann, J.; Lörzer, J.; Spittler, M.; Wiesen, P.; Ackermann, R.; Geyer, A.; Platt, U. Investigations of emissions and heterogeneous formation of HONO in a road traffic tunnel. *Atmos. Environ.* **2001**, *35*, 3385–3394, https://doi.org/10.1016/s1352-2310(01)00138-8.
16. Li, M.; Zhang, Q.; Kurokawa, J.-I.; Woo, J.-H.; He, K.; Lu, Z.; Ohara, T.; Song, Y.; Streets, D.G.; Carmichael, G.R.; et al. MIX: A mosaic Asian anthropogenic emission inventory under the international collaboration framework of the MICS-Asia and HTAP. *Atmos. Chem. Phys. Discuss.* **2017**, *17*, 935–963, https://doi.org/10.5194/acp-17-935-2017.
17. Zhang, X.; Gao, B.; Creamer, A.E.; Cao, C.; Li, Y. Adsorption of VOCs onto engineered carbon materials: A review. *J. Hazard. Mater.* **2017**, *338*, 102–123, https://doi.org/10.1016/j.jhazmat.2017.05.013.
18. Liu, Y.; Shao, M.; Fu, L.; Lu, S.; Zeng, L.; Tang, D. Source profiles of volatile organic compounds (VOCs) measured in China: Part I. *Atmos. Environ.* **2008**, *42*, 6247–6260, https://doi.org/10.1016/j.atmosenv.2008.01.070.
19. Darcovich, K.; Jonasson, K.; Capes, C. Developments in the control of fine particulate air emissions. *Adv. Powder Technol.* **1997**, *8*, 179–215, https://doi.org/10.1016/s0921-8831(08)60463-x.
20. Lasek, J.; Yu, Y.-H.; Wu, J.C.S. Removal of NOx by photocatalytic processes. *J. Photochem. Photobiol. C Photochem. Rev.* **2013**, *14*, 29–52, https://doi.org/10.1016/j.jphotochemrev.2012.08.002.
21. Xu, L.; Cheng, L.; Ji, J.; Wang, Q.; Fang, M. comprehensive CFD combustion model for supercritical CFB boilers. *Particuology* **2019**, *43*, 29–37.
22. LArmesto; Bahillo, A.; Cabanillas, A.; Veijonen, K.; Otero, J.; Plumed, A.; Salvador, L. Co-combustion of coal and olive oil industry residues in fluidised bed. *Fuel* **2003**, *82*, 993–1000.
23. Krzywanski, J.; Czakiert, T.; Shimizu, T.; Majchrzak-Kuceba, I.; Shimazaki, Y.; Zylka, A.; Grabowska, K.; Sosnowski, M. NO_x Emissions from Regenerator of Calcium Looping Process. *Energy Fuels* **2018**, *32*, 6355–6362, https://doi.org/10.1021/acs.energyfuels.8b00944.
24. Krzywanski, J.; Żyłka, A.; Czakiert, T.; Kulicki, K.; Jankowska, S.; Nowak, W. A 1.5D model of a complex geometry laboratory scale fuidized bed clc equipment. *Powder Technol.* **2017**, *316*, 592–598, https://doi.org/10.1016/j.powtec.2016.09.041.
25. Heck, R.M. Catalytic abatement of nitrogen oxides–stationary applications. *Catal. Today* **1999**, *53*, 519–523, https://doi.org/10.1016/s0920-5861(99)00139-x.
26. Kamal, M.S.; Razzak, S.; Hossain, M.M. Catalytic oxidation of volatile organic compounds (VOCs)—A review. *Atmos. Environ.* **2016**, *140*, 117–134, https://doi.org/10.1016/j.atmosenv.2016.05.031.
27. Mudliar, S.; Giri, B.S.; Padoley, K.; Satpute, D.; Dixit, R.; Bhatt, P.; Pandey, R.; Juwarkar, A.; Vaidya, A. Bioreactors for treatment of VOCs and odours—A review. *J. Environ. Manag.* **2010**, *91*, 1039–1054, https://doi.org/10.1016/j.jenvman.2010.01.006.
28. Mizuno, A. Electrostatic precipitation. *IEEE Trans. Dielectr. Electr. Insul.* **2000**, *7*, 615–624.
29. Mukhopadhyay, A. Pulse-jet filtration: An effective way to control industrial pollution Part I: Theory, selection and design of pulse-jet filter. *Text. Prog.* **2009**, *41*, 195–315, https://doi.org/10.1080/00405160903437948.
30. Granger, P.; Parvulescu, V.I. Catalytic NOx abatement systems for mobile sources: From three-way to lean burn after-treatment technologies. *Chem. Rev.* **2011**, *111*, 3155–3207.
31. Yi, F.-Y.; Lin, X.-D.; Chen, S.-X.; Wei, X.-Q. Adsorption of VOC on modified activated carbon fiber. *J. Porous Mater.* **2008**, *16*, 521–526, https://doi.org/10.1007/s10934-008-9228-5.

32. Liu, C.; Hsu, P.-C.; Lee, H.-W.; Ye, M.; Zheng, G.; Liu, N.; Li, W.; Cui, Y. Transparent air filter for high-efficiency $PM_{2.5}$ capture. *Nat. Commun.* **2015**, *6*, 6205, https://doi.org/10.1038/ncomms7205.
33. Feng, Y.; Ling, L.; Nie, J.; Han, K.; Chen, X.; Bian, Z.; Li, H.; Wang, Z.L. Self-powered electrostatic filter with enhanced photocatalytic degradation of formaldehyde based on built-in triboelectric nanogenerators. *ACS Nano* **2017**, *11*, 12411–12418.
34. Xu, J.; Liu, C.; Hsu, P.-C.; Liu, K.; Zhang, R.; Liu, Y.; Cui, Y. Roll-to-Roll Transfer of Electrospun Nanofiber Film for High-Efficiency Transparent Air Filter. *Nano Lett.* **2016**, *16*, 1270–1275, https://doi.org/10.1021/acs.nanolett.5b04596.
35. Wang, S.; Zhao, X.; Yin, X.; Yu, J.; Ding, B. Electret Polyvinylidene Fluoride Nanofibers Hybridized by Polytetrafluoroethylene Nanoparticles for High-Efficiency Air Filtration. *ACS Appl. Mater. Interfaces* **2016**, *8*, 23985–23994, https://doi.org/10.1021/acsami.6b08262.
36. Kim, J.; Hong, S.C.; Bae, G.N.; Jung, J.H. Electrospun Magnetic Nanoparticle-Decorated Nanofiber Filter and Its Applications to High-Efficiency Air Filtration. *Environ. Sci. Technol.* **2017**, *51*, 11967–11975, https://doi.org/10.1021/acs.est.7b02884.
37. Kadam, V.; Truong, Y.B.; Easton, C.; Mukherjee, S.; Wang, L.; Padhye, R.; Kyratzis, I.L. Electrospun polyacryloni-trile/β-cyclodextrin composite membranes for simultaneous air filtration and adsorption of volatile organic compounds. *ACS Appl. Nano Mater.* **2018**, *1*, 4268–4277.
38. Lv, D.; Wang, R.; Tang, G.; Mou, Z.; Lei, J.; Han, J.; de Smedt, S.; Xiong, R.; Huang, C. Ecofriendly electrospun membranes loaded with visible-light responding nanoparticles for multifunctional usages: Highly efficient air filtration, dye scavenging, and bactericidal activity. *ACS Appl. Mater. Interfaces* **2019**, *11*, 12880–12889.
39. Zou, W.; Gao, B.; Ok, Y.S.; Dong, L. Integrated adsorption and photocatalytic degradation of volatile organic compounds (VOCs) using carbon-based nanocomposites: A critical review. *Chemosphere* **2018**, *218*, 845–859, https://doi.org/10.1016/j.chemosphere.2018.11.175.
40. Yao, H.C.; Shelef, M. The surface interaction of O2 and NO with manganous oxide. *J. Catal.* **1973**, *31*, 377–383.
41. Winter, E. The catalytic decomposition of nitric oxide by metallic oxides. *J. Catal.* **1971**, *22*, 158–170, https://doi.org/10.1016/0021-9517(71)90182-5.
42. Otto, K.; Shelef, M. The adsorption of nitric oxide on iron oxides. *J. Catal.* **1970**, *18*, 184–192.
43. Chiang, Y.-C.; Chiang, P.-C.; Huang, C.-P. Effects of pore structure and temperature on VOC adsorption on activated carbon. *Carbon* **2001**, *39*, 523–534, https://doi.org/10.1016/s0008-6223(00)00161-5.
44. Lillo-Rodenas, M.A.; Cazorla-Amoros, D.; Linares-Solano, A. Behaviour of activated carbons with different pore size distributions and surface oxygen groups for benzene and toluene adsorption at low concentrations. *Carbon* **2005**, *43*, 1758–1767.
45. Wang, H.; Lashaki, M.J.; Fayaz, M.; Hashisho, Z.; Philips, J.H.; Anderson, J.E.; Nichols, M. Adsorption and desorption of mixtures of organic vapors on beaded activated carbon. *Environ. Sci. Technol.* **2012**, *46*, 8341–8350.
46. Lee, K.J.; Shiratori, N.; Lee, G.H.; Miyawaki, J.; Mochida, I.; Yoon, S.-H.; Jang, J. Activated carbon nanofiber produced from electrospun polyacrylonitrile nanofiber as a highly efficient formaldehyde adsorbent. *Carbon* **2010**, *48*, 4248–4255, https://doi.org/10.1016/j.carbon.2010.07.034.
47. Baur, G.B.; Yuranov, I.; Kiwi-Minsker, L. Activated carbon fibers modified by metal oxide as effective structured adsorbents for acetaldehyde. *Catal. Today* **2015**, *249*, 252–258, https://doi.org/10.1016/j.cattod.2014.11.021.
48. Iijima, S. Helical microtubules of graphitic carbon. *Nature* **1991**, *354*, 56–58, https://doi.org/10.1038/354056a0.
49. Shih, Y.-H.; Li, M.-S. Adsorption of selected volatile organic vapors on multiwall carbon nanotubes. *J. Hazard. Mater.* **2008**, *154*, 21–28, https://doi.org/10.1016/j.jhazmat.2007.09.095.
50. Yousefi, N.; Lu, X.; Elimelech, M.; Tufenkji, N. Environmental performance of graphene-based 3D macrostructures. *Nat. Nanotechnol.* **2019**, *14*, 107–119, https://doi.org/10.1038/s41565-018-0325-6.
51. Shen, Y.; Fang, Q.; Chen, B. Environmental Applications of Three-Dimensional Graphene-Based Macrostructures: Adsorption, Transformation, and Detection. *Environ. Sci. Technol.* **2014**, *49*, 67–84, https://doi.org/10.1021/es504421y.
52. Chabot, V.; Higgins, D.; Yu, A.; Xiao, X.; Chen, Z.; Zhang, J. A review of graphene and graphene oxide sponge: Material synthesis and applications to energy and the environment. *Energy Environ. Sci.* **2014**, *7*, 1564–1596.
53. Hu, M.; Hui, K.S. Role of graphene in MnO_2/graphene composite for catalytic ozonation of gaseous toluene. *Chem. Eng. J.* **2014**, *254*, 237–244, https://doi.org/10.1016/j.cej.2014.05.099.
54. Takeuchi, K.; Ibusuk, T. Heterogeneous photochemical reactions of a propylene-nitrogen dioxide-metal oxide-dry air system. *Atmos. Environ.* **1986**, *20*, 1155–1160.
55. Ibusuki, T.; Takeuchi, K. Removal of low concentration nitrogen oxides through photoassisted heterogeneous catalysis. *J. Mol. Catal.* **1994**, *88*, 93–102, https://doi.org/10.1016/0304-5102(93)e0247-e.
56. Paz, Y. Application of TiO_2 photocatalysis for air treatment: Patents' overview. *Appl. Catal. B Environ.* **2010**, *99*, 448–460, https://doi.org/10.1016/j.apcatb.2010.05.011.
57. Fujishima, A.; Honda, K. Electrochemical Photolysis of Water at a Semiconductor Electrode. *Nature* **1972**, *238*, 37–38, https://doi.org/10.1038/238037a0.
58. Xu, C.; Anusuyadevi, P.R.; Aymonier, C.; Luque, R.; Marre, S. Nanostructured materials for photocatalysis. *Chem. Soc. Rev.* **2019**, *48*, 3868–3902, https://doi.org/10.1039/c9cs00102f.
59. Zhang, Y.; Tang, Z.-R.; Fu, X.; Xu, Y.-J. Nanocomposite of Ag-AgBr-TiO_2 as a photoactive and durable catalyst for degradation of volatile organic compounds in the gas phase. *Appl. Catal. B Environ.* **2011**, *106*, 445–452.

60. Zhu, X.; Jin, C.; Li, X.-S.; Liu, J.-L.; Sun, Z.; Shi, C.; Li, X.; Zhu, A.-M. Photocatalytic Formaldehyde Oxidation over Plasmonic Au/TiO_2 under Visible Light: Moisture Indispensability and Light Enhancement. *ACS Catal.* **2017**, *7*, 6514–6524, https://doi.org/10.1021/acscatal.7b01658.
61. Li, J.; Dong, X.; Sun, Y.; Cen, W.; Dong, F. Facet-dependent interfacial charge separation and transfer in plasmonic photo-catalysts. *Appl. Catal. B Environ.* **2018**, *226*, 269–277.
62. Weon, S.; Choi, E.; Kim, H.; Kim, J.Y.; Park, H.-J.; Kim, S.-m.; Kim, W.; Choi, W. Active {001} facet exposed TiO_2 nanotubes photocatalyst filter for volatile organic compounds removal: From material development to commercial indoor air cleaner application. *Environ. Sci. Technol.* **2018**, *52*, 9330–9340.
63. Li, P.; Kim, S.; Jin, J.; Chun, D.H.; Park, J.H. Efficient photodegradation of volatile organic compounds by iron-based met-al-organic frameworks with high adsorption capacity. *Appl. Catal. B Environ.* **2020**, *263*, 118284–118293.
64. Wang, Z.; Chen, M.; Huang, Y.; Shi, X.; Zhang, Y.; Huang, T.; Cao, J.; Ho, W.; Lee, S.-C. Self-assembly synthesis of boron-doped graphitic carbon nitride hollow tubes for enhanced photocatalytic NOx removal under visible light. *Appl. Catal. B Environ.* **2018**, *239*, 352–361, https://doi.org/10.1016/j.apcatb.2018.08.030.
65. Weon, S.; Kim, J.; Choi, W. Dual-components modified TiO_2 with Pt and fluoride as deactivation-resistant photocatalyst for the degradation of volatile organic compound. *Appl. Catal. B Environ.* **2018**, *220*, 1–8, https://doi.org/10.1016/j.apcatb.2017.08.036.
66. Huang, Y.; Liang, Y.; Rao, Y.; Zhu, D.; Cao, J.-J.; Shen, Z.; Ho, W.; Lee, S.-C. Environment-Friendly Carbon Quantum Dots/$ZnFe_2O_4$ Photocatalysts: Characterization, Biocompatibility, and Mechanisms for NO Removal. *Environ. Sci. Technol.* **2017**, *51*, 2924–2933, https://doi.org/10.1021/acs.est.6b04460.
67. Gao, Y.; Huang, Y.; Li, Y.; Zhang, Q.; Cao, J.; Ho, W.; Lee, S.C. Plasmonic Bi/$ZnWO_4$ microspheres with improved photocatalytic activity on NO removal under visible light. *ACS Sustain. Chem. Eng.* **2016**, *4*, 6912–6920.
68. Luo, S.; Ke, J.; Yuan, M.; Zhang, Q.; Xie, P.; Deng, L.; Wang, S. $CuInS_2$ quantum dots embedded in Bi_2WO_6 nanoflowers for enhanced visible light photocatalytic removal of contaminants. *Appl. Catal. B Environ.* **2018**, *221*, 215–222.
69. Huang, Y.; Zhu, D.; Zhang, Q.; Zhang, Y.; Cao, J.-J.; Shen, Z.; Ho, W.; Lee, S.-C. Synthesis of a $Bi_2O_2CO_3$/$ZnFe_2O_4$ heterojunction with enhanced photocatalytic activity for visible light irradiation-induced NO removal. *Appl. Catal. B Environ.* **2018**, *234*, 70–78, https://doi.org/10.1016/j.apcatb.2018.04.039.
70. Zhou, H.; Wen, Z.; Liu, J.; Ke, J.; Duan, X.; Wang, S. Z-scheme plasmonic Ag decorated WO_3/Bi_2WO_6 hybrids for enhanced photocatalytic abatement of chlorinated-VOCs under solar light irradiation. *Appl. Catal. B Environ.* **2018**, *242*, 76–84, https://doi.org/10.1016/j.apcatb.2018.09.090.
71. Li, X.; Li, H.; Huang, Y.; Cao, J.; Huang, T.; Li, R.; Zhang, Q.; Lee, S.C.; Ho, W.K. Exploring the photocatalytic conversion mechanism of gaseous formaldehyde degradation on TiO_{2-x}-OV surface. *J. Hazard. Mater.* **2022**, *424*, 127217–127226.
72. Rao, Z.; Xie, X.; Wang, X.; Mahmood, A.; Tong, S.; Ge, M.; Sun, J. Defect Chemistry of Er^{3+}-Doped TiO_2 and Its Photocata-lytic Activity for the Degradation of Flowing Gas-Phase VOCs. *J. Phys. Chem. C* **2019**, *123*, 12321−12334.
73. Roso, M.; Boaretti, C.; Pelizzo, M.G.; Lauria, A.; Modesti, M.; Lorenzetti, A. Nanostructured Photocatalysts Based on Different Oxidized Graphenes for VOCs Removal. *Ind. Eng. Chem. Res.* **2017**, *56*, 9980–9992, https://doi.org/10.1021/acs.iecr.7b02526.
74. Xia, S.; Zhang, G.; Meng, Y.; Yang, C.; Ni, Z.; Hu, J. Kinetic and mechanistic analysis for the photodegradation of gaseous formaldehyde by core-shell CeO_2@LDHs. *Appl. Catal. B Environ.* **2020**, *278*, 119266–119279.
75. Fujishima, A.; Zhang, X.; Tryk, D. TiO_2 photocatalysis and related surface phenomena. *Surf. Sci. Rep.* **2008**, *63*, 515–582, https://doi.org/10.1016/j.surfrep.2008.10.001.
76. Chen, X.; Mao, S.S. Titanium dioxide nanomaterials: Synthesis, properties, modifications, and applications. *Chem. Rev.* **2007**, *107*, 2891–2959.
77. Wang, Y.; Shi, R.; Lin, J.; Zhu, Y. Enhancement of photocurrent and photocatalytic activity of ZnO hybridized with graphite-like C3N4. *Energy Environ. Sci.* **2011**, *4*, 2922–2929.
78. Chen, M.; Huang, Y.; Yao, J.; Cao, J.; Liu, Y. Visible-light-driven N-$(BiO)_2CO_3$/Graphene oxide composites with improved photocatalytic activity and selectivity for NOx removal. *Appl. Surf. Sci.* **2018**, *430*, 137–144.
79. Huang, Y.; Cao, J.-J.; Kang, F.; You, S.-J.; Chang, C.-W.; Wang, Y.-F. High selectivity of visible-light-driven La-doped TiO_2 photocatalysts for NO removal. *Aerosol Air Qual. Res.* **2017**,17, 2555-2565.
80. Liu, M.; Qiu, X.; Miyauchi, M.; Hashimoto, K. Energy-Level Matching of Fe(III) Ions Grafted at Surface and Doped in Bulk for Efficient Visible-Light Photocatalysts. *J. Am. Chem. Soc.* **2013**, *135*, 10064–10072, https://doi.org/10.1021/ja401541k.
81. Herrmann, J.-M.; Disdier, J.; Pichat, P. Effect of chromium doping on the electrical and catalytic properties of powder titania under UV and visible illumination. *Chem. Phys. Lett.* **1984**, *108*, 618–622, https://doi.org/10.1016/0009-2614(84)85067-8.
82. Zhang, Q.; Huang, Y.; Xu, L.; Cao, J.; Ho, W.; Lee, S.C. Visible-light-active plasmonic Ag-$SrTiO_3$ nanocomposites for the degradation of NO in air with high selectivity. *ACS Appl. Mater. Interfaces* **2016**, *8*, 4165–4174.
83. Liu, H.; Wang, T.; Zhang, H.; Liu, G.; Li, P.; Liu, L.; Hao, D.; Ren, J.; Chang, K.; Meng, X.; et al. Room-temperature driven and visible light enhanced dehydrogenation reactions catalyzed by basic Au/$SrTiO_3$. *J. Mater. Chem. A* **2016**, *4*, 1941–1946.
84. Demchenko, A.P.; Dekaliuk, M.O. Novel fluorescent carbonic nanomaterials for sensing and imaging. *Methods Appl. Fluoresc.* **2013**, *1*, 042001, https://doi.org/10.1088/2050-6120/1/4/042001.
85. Huang, Y.; Gao, Y.; Zhang, Q.; Zhang, Y.; Cao, J.-j.; Ho, W.; Lee, S.C. Biocompatible FeOOH-Carbon quantum dots nanocomposites for gaseous NO_x removal under visible light: Improved charge separation and high selectivity. *J. Hazard. Mater.* **2018**, *354*, 54–62.

86. Yu, X.; Liu, J.; Yu, Y.; Zuo, S.; Li, B. Preparation and visible light photocatalytic activity of carbon quantum dots/TiO_2 nanosheet composites. *Carbon* **2014**, *68*, 718–724, https://doi.org/10.1016/j.carbon.2013.11.053.
87. Hutton, G.A.M.; Martindale, B.C.M.; Reisner, E. Carbon dots as photosensitisers for solar-driven catalysis. *Chem. Soc. Rev.* **2017**, *46*, 6111–6123, https://doi.org/10.1039/c7cs00235a.
88. Dong, F.; Xiong, T.; Sun, Y.; Zhao, Z.; Zhou, Y.; Feng, X.; Wu, Z. A semimetal bismuth element as a direct plasmonic photocatlyst. *Chem. Commun.* **2014**, *50*, 10386–10389.
89. Kubacka, A.; Fernández-García, M.; Colón, G. Advanced nanoarchitectures for solar photocatalytic applications. *Chem. Rev.* **2012**, *112*, 1555–1614.
90. Wang, X.; Blechert, S.; Antonietti, M. Polymeric Graphitic Carbon Nitride for Heterogeneous Photocatalysis. *ACS Catal.* **2012**, *2*, 1596–1606, https://doi.org/10.1021/cs300240x.
91. Li, J.; Zhang, L.; Li, Y.; Yu, Y. Synthesis and internal electric field dependent photoreactivity of Bi_3O_4Cl single-crystalline nanosheets with high {001} facet exposure percentages. *Nanoscale* **2013**, *6*, 167–171, https://doi.org/10.1039/c3nr05246j.
92. Huang, Y.; Wang, W.; Zhang, Q.; Cao, J.; Huang, R.; Ho, W.; Lee, S.C. In situ fabrication of α-Bi_2O_3/$(BiO)_2CO_3$ nanoplate heterojunctions with tunable optical property and photocatalytic activity. *Sci. Rep.* **2016**, *6*, 23435.
93. Wang, Z.; Huang, Y.; Chen, L.; Chen, M.; Cao, J.; Ho, W.; Lee, S.C. In situ g-C_3N_4 self-sacrificial synthesis of a g-C_3N_4/$LaCO_3OH$ heterostructure with strong interfacial charge transfer and separation for photocatalytic NO removal. *J. Mater. Chem. A* **2017**, *6*, 972–981, https://doi.org/10.1039/c7ta09132j.
94. Wang, Z.; Huang, Y.; Ho, W.; Cao, J.; Shen, Z.; Lee, S.C. Fabrication of $Bi_2O_2CO_3$/g-C_3N_4 heterojunctions for efficiently photocatalytic NO in air removal: In-situ self-sacrificial synthesis, characterizations and mechanistic study. *Appl. Catal. B Environ.* **2016**, *199*, 123–133.
95. Low, J.; Yu, J.; Jaroniec, M.; Wageh, S.; Al-Ghamdi, A.A. Heterojunction photocatalysts. *Adv. Mater.* **2017**, *29*, 1601694.
96. Zhang, Q.; Huang, Y.; Peng, S.; Zhang, Y.; Shen, Z.; Cao, J.-J.; Ho, W.; Lee, S.-C.; Pui, D.Y. Perovskite $LaFeO_3$-$SrTiO_3$ composite for synergistically enhanced NO removal under visible light excitation. *Appl. Catal. B Environ.* **2016**, *204*, 346–357, https://doi.org/10.1016/j.apcatb.2016.11.052.
97. Mao, C.; Cheng, H.; Tian, H.; Li, H.; Xiao, W.-J.; Xu, H.; Zhao, J.; Zhang, L. Visible light driven selective oxidation of amines to imines with BiOCl: Does oxygen vacancy concentration matter? *Appl. Catal. B Environ.* **2018**, *228*, 87–96.
98. Zhang, Q.; Huang, Y.; Peng, S.; Huang, T.; Cao, J.-J.; Ho, W.; Lee, S.-C. Synthesis of $SrFe_xTi_{1-x}O_{3-\delta}$ nanocubes with tunable oxygen vacancies for selective and efficient photocatalytic NO oxidation. *Appl. Catal. B Environ.* **2018**, *239*, 1–9, https://doi.org/10.1016/j.apcatb.2018.07.076.
99. Tasbihi, M.; Štangar, U.L.; Černigoj, U.; Jirkovsky, J.; Bakardjieva, S.; Tušar, N.N. Photocatalytic oxidation of gaseous toluene on titania/mesoporous silica powders in a fluidized-bed reactor. *Catal. Today* **2011**, *161*, 181–188.
100. Ahmad, R.; Kim, J.K.; Kim, J.H.; Kim, J. Well-organized, mesoporous nanocrystalline TiO_2 on alumina membranes with hierarchical architecture: Antifouling and photocatalytic activities. *Catal. Today* **2017**, *282*, 2–12.
101. Gomez, S.; Marchena, C.L.; Renzini, M.S.; Pizzio, L.; Pierella, L. In situ generated TiO_2 over zeolitic supports as reusable photocatalysts for the degradation of dichlorvos. *Appl. Catal. B Environ.* **2015**, *162*, 167–173.
102. Zhang, Y.; Tang, Z.-R.; Fu, X.; Xu, Y.-J. TiO_2-graphene nanocomposites for gas-phase photocatalytic degradation of volatile aromatic pollutant: Is TiO_2-graphene truly different from other TiO_2-carbon composite materials? *ACS Nano* **2010**, *4*, 7303–7314.
103. Li, M.; Lu, B.; Ke, Q.-F.; Guo, Y.-J. Synergetic effect between adsorption and photodegradation on nanostructured TiO_2/activated carbon fiber felt porous composites for toluene removal. *J. Hazard. Mater.* **2017**, *333*, 88–98, https://doi.org/10.1016/j.jhazmat.2017.03.019.
104. Martins, A.C.; Cazetta, A.L.; Pezoti, O.; de Souza, J.R.B.; Zhang, T.; Pilau, E.; Asefa, T.; Almeida, V.C. Sol-gel synthesis of new TiO_2/activated carbon photocatalyst and its application for degradation of tetracycline. *Ceram. Int.* **2017**, *43*, 4411–4418, https://doi.org/10.1016/j.ceramint.2016.12.088.
105. Shan, A.Y.; Ghazi, T.I.M.; Rashid, S.A. Immobilization of titanium dioxide onto supporting materials in heterogeneous photocatalysis: A review. *Appl. Catal. A Gen.* **2010**, *389*, 1–8.
106. Behnajady, M.A.; Modirshahla, N.; Hamzavi, R. Kinetic study on photocatalytic degradation of C.I. Acid Yellow 23 by ZnO photocatalyst. *J. Hazard. Mater.* **2006**, *133*, 226–232, https://doi.org/10.1016/j.jhazmat.2005.10.022.
107. Stafford, U.; Gray, K.A.; Kamat, P. Photocatalytic Degradation of 4-Chlorophenol: The Effects of Varying TiO_2 Concentration and Light Wavelength. *J. Catal.* **1997**, *167*, 25–32, https://doi.org/10.1006/jcat.1997.1511.
108. Ohko, Y.; Hashimoto, K.; Fujishima, A. Kinetics of Photocatalytic Reactions under Extremely Low-Intensity UV Illumination on Titanium Dioxide Thin Films. *J. Phys. Chem. A* **1997**, *101*, 8057–8062, https://doi.org/10.1021/jp972002k.
109. Hoffmann, M.R.; Martin, S.T.; Choi, W.; Bahnemann, D.W. Environmental Applications of Semiconductor Photocatalysis. *Chem. Rev.* **1995**, *95*, 69–96, https://doi.org/10.1021/cr00033a004.
110. Emeline, A.V.; Ryabchuk, V.K.; Serpone, N. Dogmas and Misconceptions in Heterogeneous Photocatalysis. Some Enlightened Reflections. *J. Phys. Chem. B* **2005**, *109*, 18515–18521, https://doi.org/10.1021/jp0523367.
111. Moulis, F.; Krýsa, J. Photocatalytic degradation of several VOCs (n-hexane, n-butyl acetate and toluene) on TiO_2 layer in a closed-loop reactor. *Catal. Today* **2012**, *209*, 153–158, https://doi.org/10.1016/j.cattod.2012.10.017.
112. Zhong, L.; Haghighat, F.; Lee, C.-S.; Lakdawala, N. Performance of ultraviolet photocatalytic oxidation for indoor air applications: Systematic experimental evaluation. *J. Hazard. Mater.* **2013**, *261*, 130–138.

113. Mo, J.; Zhang, Y.; Xu, Q.; Yang, R. Effect of TiO_2/adsorbent hybrid photocatalysts for toluene decomposition in gas phase. *J. Hazard. Mater.* **2009**, *168*, 276–281, https://doi.org/10.1016/j.jhazmat.2009.02.033.
114. Debono, O.; Thevenet, F.; Gravejat, P.; Hequet, V.; Raillard, C.; LE Coq, L.; Locoge, N. Toluene photocatalytic oxidation at ppbv levels: Kinetic investigation and carbon balance determination. *Appl. Catal. B Environ.* **2011**, *106*, 600–608, https://doi.org/10.1016/j.apcatb.2011.06.021.
115. Zhang, L.; Anderson, W.A.; Sawell, S.; Moralejo, C. Mechanistic analysis on the influence of humidity on photocatalytic decomposition of gas-phase chlorobenzene. *Chemosphere* **2007**, *68*, 546–553.
116. Peral, J.; Ollis, D.F. Heterogeneous photocatalytic oxidation of gas-phase organics for air purification: Acetone, 1-butanol, butyraldehyde, formaldehyde, and m-xylene oxidation. *J. Catal.* **1992**, *136*, 554–565, https://doi.org/10.1016/0021-9517(92)90085-v.
117. Cao, L.; Spiess, F.-J.; Huang, A.; Suib, S.L.; Obee, T.N.; Hay, S.O.; Freihaut, J.D. Heterogeneous Photocatalytic Oxidation of 1-Butene on SnO_2 and TiO_2 Films. *J. Phys. Chem. B* **1999**, *103*, 2912–2917, https://doi.org/10.1021/jp983860z.
118. Sleiman, M.; Conchon, P.; Ferronato, C.; Chovelon, J.-M. Photocatalytic oxidation of toluene at indoor air levels (ppbv): Towards a better assessment of conversion, reaction intermediates and mineralization. *Appl. Catal. B Environ.* **2009**, *86*, 159–165.
119. Lichtin, N.N.; Avudaithai, M.; Berman, E.; Grayfer, A. TiO_2-photocatalyzed oxidative degradation of binary mixtures of vaporized organic compounds. *Sol. Energy* **1996**, *56*, 377–385.
120. Ao, C.; Lee, S.; Yu, J.Z.; Xu, J. Photodegradation of formaldehyde by photocatalyst TiO_2: Effects on the presences of NO, SO_2 and VOCs. *Appl. Catal. B Environ.* **2004**, *54*, 41–50, https://doi.org/10.1016/j.apcatb.2004.06.004.
121. Stucchi, M.; Galli, F.; Bianchi, C.; Pirola, C.; Boffito, D.C.; Biasioli, F.; Capucci, V. Simultaneous photodegradation of VOC mixture by TiO_2 powders. *Chemosphere* **2018**, *193*, 198–206, https://doi.org/10.1016/j.chemosphere.2017.11.003.
122. Debono, O.; Hequet, V.; Le Coq, L.; Locoge, N.; Thevenet, F. VOC ternary mixture effect on ppb level photocatalytic oxidation: Removal kinetic, reaction intermediates and mineralization. *Appl. Catal. B Environ.* **2017**, *218*, 359–369, https://doi.org/10.1016/j.apcatb.2017.06.070.
123. Cao, L.; Gao, Z.; Suib, S.L.; Obee, T.N.; Hay, S.O.; Freihaut, J.D. Photocatalytic Oxidation of Toluene on Nanoscale TiO_2 Catalysts: Studies of Deactivation and Regeneration. *J. Catal.* **2000**, *196*, 253–261, https://doi.org/10.1006/jcat.2000.3050.
124. Liu, L.; Zhang, X.; Yang, L.; Ren, L.; Wang, D.; Ye, J. Metal nanoparticles induced photocatalysis. *Natl. Sci. Rev.* **2017**, *4*, 761–780, https://doi.org/10.1093/nsr/nwx019.
125. Cui, W.; Li, J.; Dong, F.; Sun, Y.; Jiang, G.; Cen, W.; Lee, S.C.; Wu, Z. Highly efficient performance and conversion pathway of photocatalytic NO oxidation on SrO-clusters@amorphous carbon nitride. *Environ. Sci. Technol.* **2017**, *51*, 10682–10690.
126. Li, X.; Zhang, W.; Li, J.; Jiang, G.; Zhou, Y.; Lee, S.; Dong, F. Transformation pathway and toxic intermediates inhibition of photocatalytic NO removal on designed Bi metal@defective $Bi_2O_2SiO_3$. *Appl. Catal. B Environ.* **2019**, *241*, 187–195.
127. Li, X.; Xu, Y.; Zhang, C.; Wang, H.; Song, Y.; Zhang, W.; Li, C. H_2O_2-assisted hydrothermal synthesis of TiO_2-SiO_2 and its enhanced photocatalytic-adsorptive desulfurization performance for model fuel. *Fuel* **2018**, *226*, 527–535.
128. Li, H.; Shang, H.; Cao, X.; Yang, Z.; Ai, Z.; Zhang, L. Oxygen Vacancies Mediated Complete Visible Light NO Oxidation via Side-On Bridging Superoxide Radicals. *Environ. Sci. Technol.* **2018**, *52*, 8659–8665, https://doi.org/10.1021/acs.est.8b01849.
129. Chen, P.; Sun, Y.; Liu, H.; Zhou, Y.; Jiang, G.; Lee, S.C.; Zhang, Y.; Dong, F. Facet-dependent photocatalytic NO conversion pathways predetermined by adsorption activation patterns. *Nanoscale* **2019**, *11*, 2366–2373, https://doi.org/10.1039/c8nr09147a.
130. Dong, X.; Li, J.; Xing, Q.; Zhou, Y.; Huang, H.; Dong, F. The activation of reactants and intermediates promotes the selective photocatalytic NO conversion on electron-localized Sr-intercalated g-C_3N_4. *Appl. Catal. B Environ.* **2018**, *232*, 69–76, https://doi.org/10.1016/j.apcatb.2018.03.054.
131. Weon, S.; Choi, W. TiO_2 Nanotubes with Open Channels as Deactivation-Resistant Photocatalyst for the Degradation of Volatile Organic Compounds. *Environ. Sci. Technol.* **2016**, *50*, 2556–2563, https://doi.org/10.1021/acs.est.5b05418.
132. Pillai, U.R.; Sahle-Demessie, E. Selective Oxidation of Alcohols in Gas Phase Using Light-Activated Titanium Dioxide. *J. Catal.* **2002**, *211*, 434–444, https://doi.org/10.1006/jcat.2002.3771.
133. Piera, E.; Ayllon, J.A.; Doménech, X.; Peral, J. TiO_2 deactivation during gas-phase photocatalytic oxidation of ethanol. *Catal. Today* **2002**, *76*, 259–270, https://doi.org/10.1016/s0920-5861(02)00224-9.
134. Ameen, M.; Raupp, G.B. Reversible Catalyst Deactivation in the Photocatalytic Oxidation of Diluteo-Xylene in Air. *J. Catal.* **1999**, *184*, 112–122, https://doi.org/10.1006/jcat.1999.2442.
135. Ma, Y.; Zhang, G. Sepiolite nanofiber-supported platinum nanoparticle catalysts toward the catalytic oxidation of formaldehyde at ambient temperature: Efficient and stable performance and mechanism. *Chem. Eng. J.* **2016**, *288*, 70–78.
136. Jiaguo, Y.; Xinyang, L.; Zhihua, X.; Wei, X. NaOH-modified ceramic honeycomb with enhanced formaldehyde adsorption and removal performance. *Environ. Sci. Technol.* **2013**, *47*, 9928–9933.
137. Pei, J.; Zhang; Jianshun, S. On the performance and mechanisms of formaldehyde removal by chemi-sorbents. *Chem. Eng. J.* **2011**, *167*, 59–66.
138. Nakayama, H.; Hayashi, A.; Eguchi, T.; Nakamura, N.; Tsuhako, M. Adsorption of formaldehyde by polyamine-intercalated α-zirconium phosphate. *Solid State Sci.* **2002**, *4*, 1067–1070, https://doi.org/10.1016/s1293-2558(02)01367-5.
139. Bai, B.; Arandiyan, H.; Li, J. Comparison of the performance for oxidation of formaldehyde on nano-Co_3O_4, 2D-Co_3O_4, and 3D-Co_3O_4 catalysts. *Appl. Catal. B Environ.* **2013**, *142–143*, 677–683, https://doi.org/10.1016/j.apcatb.2013.05.056.
140. Chen, H.; He, J.; Zhang, A.C.; He, H. Self-Assembly of Novel Mesoporous Manganese Oxide Nanostructures and Their Application in Oxidative Decomposition of Formaldehyde. *J. Phys. Chem. C* **2007**, *111*, 18033–18038, https://doi.org/10.1021/jp076113n.

141. Wang, J.; Zhang, P.; Li, J.; Jiang, C.; Yunus, R.; Kim, J. Room-temperature oxidation of formaldehyde by layered manganese oxide: Effect of water. *Environ. Sci. Technol.* **2015**, *49*, 12372.
142. Rong, S.; Zhang, P.; Yang, Y.; Lin, Z.; Wang, J.; Fang, L. MnO_2 framework for instantaneous mineralization of carcinogenic airborne formaldehyde at room temperature. *ACS Catal.* **2017**, *7*, 1057–1067.
143. Sidheswaran, M.A.; Destaillats, H.; Sullivan, D.P.; Larsen, J.; Fisk, W.J. Quantitative room-temperature mineralization of airborne formaldehyde using manganese oxide catalysts. *Appl. Catal. B Environ.* **2011**, *107*, 34–41.
144. Foster, J.J.; Masel, R.I. Formaldehyde oxidation on nickel oxide. *Ind. Eng. Chem. Prod. Res. Dev.* **1986**, *25*, 563–568, https://doi.org/10.1021/i300024a010.
145. Yu, X.; Zhang, Z.; Yang, C.; Bebensee, F.; Heissler, S.; Nefedov, A.; Tang, M.; Ge, Q.; Long, C.; Kay, B.D. Interaction of formaldehyde with the rutile TiO_2(110) surface: A combined experimental and theoretical study. *J. Phys. Chem. C* **2016**, *120*, 12626–12636.
146. Yu, X.; He, J.; Wang, D.; Hu, Y.; Hua, T.; He, Z. Facile controlled synthesis of Pt/MnO_2 nanostructured catalysts and their catalytic performance for oxidative decomposition of formaldehyde. *J. Phys. Chem. C* **2011**, *116*, 851–860.
147. Zhang, C.; He, H. A comparative study of TiO_2 supported noble metal catalysts for the oxidation of formaldehyde at room temperature. *Catal. Today* **2007**, *126*, 345–350, https://doi.org/10.1016/j.cattod.2007.06.010.
148. Changbin, Z.; Fudong, L.; Yanping, Z.; Hiroko, A.; Nan, Y.; Yongchun, L.; Kiyotaka, A.; Maria, F.S.; Hong, H. Alka-li-metal-promoted Pt/TiO_2 opens a more efficient pathway to formaldehyde oxidation at ambient temperatures. *Angew. Chem. Int.* **2012**, *51*, 9628–9632.
149. Bai, B.; Li, J. Positive Effects of K^+ Ions on Three-Dimensional Mesoporous Ag/Co_3O_4 Catalyst for HCHO Oxidation. *ACS Catal.* **2014**, *4*, 2753–2762, https://doi.org/10.1021/cs5006663.
150. Chen, B.B.; Zhu, X.B.; Crocker, M.; Yu, W.; Shi, C. FeOx-supported gold catalysts for catalytic removal of formaldehyde at room temperature. *Appl. Catal. B: Environ.* 2014, 154-155, 73-81.
151. Huang, H.Y.; Yang, R.T. Removal of NO by Reversible Adsorption on Fe−Mn Based Transition Metal Oxides. *Langmuir* **2001**, *17*, 4997–5003, https://doi.org/10.1021/la0102657.
152. Sekine, Y. Oxidative decomposition of formaldehyde by metal oxides at room temperature. *Atmos. Environ.* **2002**, *36*, 5543–5547, https://doi.org/10.1016/s1352-2310(02)00670-2.
153. Zhang, J.; Li, Y.; Wang, L.; Zhang, C.; He, H. Catalytic oxidation of formaldehyde over manganese oxides with different crystal structures. *Catal. Sci. Technol.* **2015**, *5*, 2305–2313, https://doi.org/10.1039/c4cy01461h.
154. Bai, B.; Qiao, Q.; Arandiyan, H.; Li, J.; Hao, J. Three-Dimensional Ordered Mesoporous MnO_2-Supported Ag Nanoparticles for Catalytic Removal of Formaldehyde. *Environ. Sci. Technol.* **2016**, *50*, 2635–2640, https://doi.org/10.1021/acs.est.5b03342.
155. Zhang, C.; He, H.; Tanaka, K.-I. Catalytic performance and mechanism of a Pt/TiO_2 catalyst for the oxidation of formaldehyde at room temperature. *Appl. Catal. B Environ.* **2006**, *65*, 37–43, https://doi.org/10.1016/j.apcatb.2005.12.010.
156. Li, G.; Li, L. Highly efficient formaldehyde elimination over meso-structured M/CeO2 (M = Pd, Pt, Au and Ag) catalyst under ambient conditions. *RSC Adv.* **2015**, *5*, 36428–36433, https://doi.org/10.1039/c5ra04928h.
157. An, N.; Wu, P.; Li, S.; Jia, M.; Zhang, W. Catalytic oxidation of formaldehyde over Pt/Fe_2O_3 catalysts prepared by different method. *Appl. Surf. Sci.* **2013**, *285*, 805–809, https://doi.org/10.1016/j.apsusc.2013.08.132.
158. Ikegami, M.; Matsumoto, T.; Kobayashi, Y.; Jikihara, Y.; Nakayama, T.; Ohashi, H.; Honma, T.; Takei, T.; Haruta, M. Air purification by gold catalysts supported on PET nonwoven fabric. *Appl. Catal. B Environ.* **2013**, *134–135*, 130–135.
159. Shu, Z.; Huang, W.; Hua, Z.; Zhang, L.; Cui, X.; Chen, Y.; Chen, H.; Wei, C.; Wang, Y.; Fan, X.; et al. Template-free synthesis of mesoporous X–Mn (X = Co, Ni, Zn) bimetal oxides and catalytic application in the room temperature removal of low-concentration NO. *J. Mater. Chem. A* **2013**, *1*, 10218–10227, https://doi.org/10.1039/c3ta10971b.
160. Shu, Z.; Chen, Y.; Huang, W.; Cui, X.; Zhang, L.; Chen, H.; Zhang, G.; Fan, X.; Wang, Y.; Tao, G.; et al. Room-temperature catalytic removal of low-concentration NO over mesoporous Fe–Mn binary oxide synthesized using a template-free approach. *Appl. Catal. B Environ.* **2013**, *140–141*, 42–50, https://doi.org/10.1016/j.apcatb.2013.03.030.
161. Huang, W.; Shi, J. Water-promoted low-concentration NO removal at room temperature by Mg-doped manganese oxides OMS-2. *Appl. Catal. A Gen.* **2015**, *507*, 65–74, https://doi.org/10.1016/j.apcata.2015.09.015.
162. Wang, J.; Zhu, J.; Zhou, X.; Du, Y.; Huang, W.; Liu, J.; Zhang, W.; Shi, J.; Chen, H. Nanoflower-like weak crystallization manganese oxide for efficient removal of low-concentration NO at room temperature. *J. Mater. Chem. A* **2015**, *3*, 7631–7638.
163. Du, Y.; Hua, Z.; Huang, W.; Wu, M.; Wang, M.; Wang, J.; Cui, X.; Zhang, L.; Chen, H.; Shi, J. Mesostructured amorphous manganese oxides: Facile synthesis and highly durable elimination of low-concentration NO at room temperature in air. *Chem. Commun.* **2015**, *51*, 5887–5889.
164. Mochida, I.; Kawabuchi, Y.; Kawano, S.; Matsumura, Y.; Yoshikawa, M. High catalytic activity of pitch-based activated carbon fibres of moderate surface area for oxidation of NO to NO_2 at room temperature. *Fuel* **1997**, *76*, 543–548, https://doi.org/10.1016/s0016-2361(96)00223-2.
165. Liu, H.; Zhang, Z.; Xu, Y.; Chen, Y.; Li, X. Adsorption-Oxidation Reaction Mechanism of NO on Na-ZSM-5 Molecular Sieves with a High Si/Al Ratio at Ambient Temperature. *Chin. J. Catal.* **2010**, *31*, 1233–1241, https://doi.org/10.1016/s1872-2067(10)60117-9.
166. Liu, S.; Zhang, M.; Huang, Y.; Zhao, K.; Gao, Z.; Wu, M.; Dong, Y.; Wang, T.; Shi, J.; He, D. A novel chromic oxide catalyst for NO oxidation at ambient temperature. *RSC Adv.* **2014**, *4*, 29180–29186, https://doi.org/10.1039/c4ra02681k.
167. Wang, A.; Guo, Y.; Gao, F.; Peden, C.H.F. Ambient-temperature NO oxidation over amorphous CrOx-ZrO_2 mixed oxide catalysts: Significant promoting effect of ZrO_2. *Appl. Catal. B Environ.* **2017**, *202*, 706–714.

168. Wang, A.; Lin, B.; Zhang, H.; Engelhard, M.H.; Guo, Y.; Lu, G.; Peden, C.H.F.; Gao, F. Ambient temperature NO oxidation over Cr-based amorphous mixed oxide catalysts: Effects from the second oxide components. *Catal. Sci. Technol.* **2017**, *7*, 2362–2370, https://doi.org/10.1039/c7cy00490g.
169. Wang, J.; Li, J.; Jiang, C.; Zhou, P.; Zhang, P.; Yu, J. The effect of manganese vacancy in birnessite-type MnO2 on room-temperature oxidation of formaldehyde in air. *Appl. Catal. B Environ.* **2017**, *204*, 147–155, https://doi.org/10.1016/j.apcatb.2016.11.036.
170. Meng, Y.; Song, W.; Huang, H.; Ren, Z.; Chen, S.-Y.; Suib, S.L. Structure-property relationship of bifunctional MnO2 nanostructures: Highly efficient, ultra-stable electrochemical water oxidation and oxygen reduction reaction catalysts identified in alkaline media. *J. Am. Chem. Soc.* **2014**, *136*, 11452–11464.
171. Chen, T.; Dou, H.; Li, X.; Tang, X.; Li, J.; Hao, J. Tunnel structure effect of manganese oxides in complete oxidation of formaldehyde. *Microporous Mesoporous Mater.* **2009**, *122*, 270–274.
172. Jia, J.; Zhang, P.; Chen, L. The effect of morphology of α-MnO2 on catalytic decomposition of gaseous ozone. *Catal. Sci. Technol.* **2016**, *6*, 5841–5847.
173. Wang, F.; Dai, H.; Deng, J.; Bai, G.; Ji, K.; Liu, Y. Manganese Oxides with Rod-, Wire-, Tube-, and Flower-Like Morphologies: Highly Effective Catalysts for the Removal of Toluene. *Environ. Sci. Technol.* **2012**, *46*, 4034–4041, https://doi.org/10.1021/es204038j.
174. Zhang, Y.; Huang, Y.; Lee, S.C.; Cao, J.-J. The mechanism of room temperature catalytic C–H dissociation and oxygenation of formaldehyde over nano-zirconia phase-junction. *Chem. Eng. J.* **2019**, *380*, 122498, https://doi.org/10.1016/j.cej.2019.122498.
175. Zhu, D.; Huang, Y.; Cao, J.-J.; Lee, S.C.; Chen, M.; Shen, Z. Cobalt nanoparticles encapsulated in porous nitrogen-doped carbon: Oxygen activation and efficient catalytic removal of formaldehyde at room temperature. *Appl. Catal. B Environ.* **2019**, *258*, https://doi.org/10.1016/j.apcatb.2019.117981.
176. Li, H.; Ho, W.; Cao, J.; Park, D.; Lee, S.-c.; Huang, Y. Active complexes on engineered crystal facets of MnOx-CeO_2 and scale-up demonstration on an air cleaner for indoor formaldehyde removal. *Environ. Sci. Technol.* **2019**, *53*, 10906–10916.
177. Du, Y.; Huang, W.; Hua, Z.; Wang, Y.; Cui, X.; Wu, M.; Shu, Z.; Zhang, L.; Wang, J.; Chen, H.; et al. A facile ultrasonic process for the preparation of Co_3O_4 nanoflowers for room-temperature removal of low-concentration NO_x. *Catal. Commun.* **2014**, *57*, 73–77, https://doi.org/10.1016/j.catcom.2014.07.040.
178. Wang, M.-X.; Huang, Z.-H.; Shimohara, T.; Kang, F.; Liang, K. NO removal by electrospun porous carbon nanofibers at room temperature. *Chem. Eng. J.* **2011**, *170*, 505–511, https://doi.org/10.1016/j.cej.2011.01.017.
179. Fujiwara, K.; Okuyama, K.; Pratsinis, S.E. Metal–support interactions in catalysts for environmental remediation. *Environ. Sci. Nano* **2017**, *4*, 2076–2092, https://doi.org/10.1039/c7en00678k.
180. Rui, Z.; Chen, L.; Chen, H.; Ji, H. Strong Metal-Support Interaction in Pt/TiO_2 Induced by Mild HCHO and $NaBH_4$ Solution Reduction and Its Effect on Catalytic Toluene Combustion. *Ind. Eng. Chem. Res.* **2014**, *53*, 15879–15888, https://doi.org/10.1021/ie5029107.
181. Xu, Q.; Lei, W.; Li, X.; Qi, X.; Yu, J.; Liu, G.; Wang, J.; Zhang, P. Efficient Removal of Formaldehyde by Nanosized Gold on Well-Defined CeO_2 Nanorods at Room Temperature. *Environ. Sci. Technol.* **2014**, *48*, 9702–9708, https://doi.org/10.1021/es5019477.
182. Vayssilov, G.N.; Lykhach, Y.; Migani, A.; Staudt, T.; Petrova, G.P.; Tsud, N.; Skála, T.; Bruix, A.; Illas, F.; Prince, K.C.; et al. Support nanostructure boosts oxygen transfer to catalytically active platinum nanoparticles. *Nat. Mater.* **2011**, *10*, 310–315.
183. Li, H.; Shang, J.; Yang, Z.; Shen, W.; Ai, Z.; Zhang, L. Oxygen Vacancy Associated Surface Fenton Chemistry: Surface Structure Dependent Hydroxyl Radicals Generation and Substrate Dependent Reactivity. *Environ. Sci. Technol.* **2017**, *51*, 5685–5694, https://doi.org/10.1021/acs.est.7b00040.
184. Huang, H.; Leung, D.Y. Complete elimination of indoor formaldehyde over supported Pt catalysts with extremely low Pt content at ambient temperature. *J. Catal.* **2011**, *280*, 60–67, https://doi.org/10.1016/j.jcat.2011.03.003.
185. Liu, B.-T.; Hsieh, C.-H.; Wang, W.-H.; Huang, C.-C.; Huang, C.-J. Enhanced catalytic oxidation of formaldehyde over dual-site supported catalysts at ambient temperature. *Chem. Eng. J.* **2013**, *232*, 434–441, https://doi.org/10.1016/j.cej.2013.08.005.
186. Park, S.J.; Bae, I.; Nam, I.-S.; Cho, B.K.; Jung, S.M.; Lee, J.-H. Oxidation of formaldehyde over Pd/Beta catalyst. *Chem. Eng. J.* **2012**, *195–196*, 392–402, https://doi.org/10.1016/j.cej.2012.04.028.
187. Chen, B.-B.; Shi, C.; Crocker, M.; Wang, Y.; Zhu, A.-M. Catalytic removal of formaldehyde at room temperature over supported gold catalysts. *Appl. Catal. B Environ.* **2013**, *132-133*, 245–255, https://doi.org/10.1016/j.apcatb.2012.11.028.
188. Chen, B.-B.; Zhu, X.; Crocker, M.; Wang, Y.; Shi, C. Complete oxidation of formaldehyde at ambient temperature over γ-Al_2O_3 supported Au catalyst. *Catal. Commun.* **2013**, *42*, 93–97, https://doi.org/10.1016/j.catcom.2013.08.008.
189. Grbic, B.; Radic, N.; Terlecki-Baricevic, A. Kinetics of deep oxidation of n-hexane and toluene over Pt/Al_2O_3 catalysts: Oxidation of mixture. *Appl. Catal. B Environ.* **2004**, *50*, 161–166, https://doi.org/10.1016/j.apcatb.2004.01.012.
190. Mars, P.; van Krevelen, D. Oxidations carried out by means of vanadium oxide catalysts. *Chem. Eng. Sci.* **1954**, *3*, 41–59, https://doi.org/10.1016/s0009-2509(54)80005-4.
191. Garetto, T.; Apesteguía, C. Oxidative catalytic removal of hydrocarbons over Pt/Al_2O_3 catalysts. *Catal. Today* **2000**, *62*, 189–199, https://doi.org/10.1016/s0920-5861(00)00420-x.
192. Doornkamp, C.; Ponec, V. The universal character of the Mars and Van Krevelen mechanism. *J. Mol. Catal. A Chem.* **2000**, *162*, 19–32, https://doi.org/10.1016/s1381-1169(00)00319-8.
193. Ma, C.; Wang, D.; Xue, W.; Dou, B.; Wang, H.; Hao, Z. Investigation of Formaldehyde Oxidation over Co_3O_4–CeO_2 and Au/Co_3O_4–CeO_2 Catalysts at Room Temperature: Effective Removal and Determination of Reaction Mechanism. *Environ. Sci. Technol.* **2011**, *45*, 3628–3634, https://doi.org/10.1021/es104146v.

194. Wu, H.; Ma, S.; Song, W.; Hensen, E.J.M. Density Functional Theory Study of the Mechanism of Formaldehyde Oxidation on Mn-Doped Ceria. *J. Phys. Chem. C* **2016**, *120*, 13071–13077, https://doi.org/10.1021/acs.jpcc.6b03218.
195. Sun, D.; Le, Y.; Jiang, C.; Cheng, B. Ultrathin Bi2WO6 nanosheet decorated with Pt nanoparticles for efficient formaldehyde removal at room temperature. *Appl. Surf. Sci.* **2018**, *441*, 429–437, https://doi.org/10.1016/j.apsusc.2018.02.001.
196. Wang, Z.; Wang, W.; Zhang, L.; Jiang, D. Surface oxygen vacancies on Co_3O_4 mediated catalytic formaldehyde oxidation at room temperature. *Catal. Sci. Technol.* **2015**, *6*, 3845–3853, https://doi.org/10.1039/c5cy01709b.
197. Yan, Z.; Xu, Z.; Yu, J.; Jaroniec, M. Highly Active Mesoporous Ferrihydrite Supported Pt Catalyst for Formaldehyde Removal at Room Temperature. *Environ. Sci. Technol.* **2015**, *49*, 6637–6644, https://doi.org/10.1021/acs.est.5b00532.
198. Jin, J.; Sun, N.; Hu, W.; Yuan, H.; Wang, H.; Hu, P. Insight into Room-Temperature Catalytic Oxidation of Nitric oxide by Cr_2O_3: A DFT Study. *ACS Catal.* **2018**, *8*, 5415–5424, https://doi.org/10.1021/acscatal.8b00081.
199. Zhu, X.; Bei, C.; Yu, J.; Ho, W. Halogen poisoning effect of Pt-TiO_2 for formaldehyde catalytic oxidation performance at room temperature. *Appl. Surf. Sci.* **2016**, *364*, 808–814.
200. Chen, B.B.; Zhu, X.B.; Wang, Y.D.; Yu, L.M.; Lu, J.Q.; Shi, C. Nano-sized gold particles dispersed on HZSM-5 and SiO_2 substrates for catalytic oxidation of HCHO. *Catal. Today* **2017**, *281*, 512–519.
201. Hauff, K.; Dubbe, H.; Tuttlies, U.; Eigenberger, G.; Nieken, U. Platinum oxide formation and reduction during NO oxidation on a diesel oxidation catalyst—Macrokinetic simulation. *Appl. Catal. B Environ.* **2013**, *129*, 273–281, https://doi.org/10.1016/j.apcatb.2012.09.022.
202. Wang, H.-F.; Guo, Y.-L.; Lu, G.; Hu, P. NO Oxidation on Platinum Group Metals Oxides: First Principles Calculations Combined with Microkinetic Analysis. *J. Phys. Chem. C* **2009**, *113*, 18746–18752, https://doi.org/10.1021/jp904371f.
203. Dong, F.; Wang, Z.; Li, Y.; Ho, W.-K.; Lee, S.C. Immobilization of Polymeric g-C_3N_4 on Structured Ceramic Foam for Efficient Visible Light Photocatalytic Air Purification with Real Indoor Illumination. *Environ. Sci. Technol.* **2014**, *48*, 10345–10353, https://doi.org/10.1021/es502290f.
204. Maynard, A.D.; Aitken, R.J.; Butz, T.; Colvin, V.; Donaldson, K.; Oberdörster, G.; Philbert, M.A.; Ryan, J.; Seaton, A.; Stone, V.; et al. Safe handling of nanotechnology. *Nature* **2006**, *444*, 267–269, https://doi.org/10.1038/444267a.
205. Peill, N.J.; Hoffmann, M.R. Development and optimization of a TiO_2-coated fiber-optic cable reactor: Photocatalytic degradation of 4-chlorophenol. *Environ. Sci. Technol.* **1995**, *29*, 2974–2981.
206. Rachel, A.; Lavedrine, B.; Subrahmanyam, M.; Boule, P. Use of porous lavas as supports of photocatalysts. *Catal. Commun.* **2002**, *3*, 165–171, https://doi.org/10.1016/s1566-7367(02)00076-6.
207. Liu, Z.; Fang, P.; Wang, S.; Gao, Y.; Chen, F.; Zheng, F.; Liu, Y.; Dai, Y. Photocatalytic degradation of gaseous benzene with CdS-sensitized TiO_2 film coated on fiberglass cloth. *J. Mol. Catal. A Chem.* **2012**, *363*, 159–165.
208. Habibi, M.H.; Mikhak, M. Titania/zinc oxide nanocomposite coatings on glass or quartz substrate for photocatalytic degradation of direct blue 71, Appl. Surf. Sci. **2012**, *258*, 6745–6752.
209. Mu, Q.; Zhang, Q.; Wang, H.; Li, Y. Facile growth of vertically aligned BiOCl nanosheet arrays on conductive glass substrate with high photocatalytic properties. *J. Mater. Chem.* **2012**, *22*, 16851–16857, https://doi.org/10.1039/c2jm32781c.
210. Yu, J.C.; Ho, W.; Lin, J.; Yip, H.; Wong, P.K. Photocatalytic Activity, Antibacterial Effect, and Photoinduced Hydrophilicity of TiO_2 Films Coated on a Stainless Steel Substrate. *Environ. Sci. Technol.* **2003**, *37*, 2296–2301, https://doi.org/10.1021/es0259483.
211. Ohko, Y.; Nakamura, Y.; Fukuda, A.; Matsuzawa, S.; Takeuchi, K. Photocatalytic Oxidation of Nitrogen Dioxide with TiO_2 Thin Films under Continuous UV-Light Illumination. *J. Phys. Chem. C* **2008**, *112*, 10502–10508, https://doi.org/10.1021/jp802959c.
212. Anderson, C.; Bard, A.J. An Improved Photocatalyst of TiO_2/SiO_2 Prepared by a Sol-Gel Synthesis. *J. Phys. Chem.* **1995**, *99*, 9882–9885, https://doi.org/10.1021/j100024a033.
213. Kato, K.; Tsuzuki, A.; Taoda, H.; Torii, Y.; Kato, T.; Butsugan, Y. Crystal structures of TiO_2 thin coatings prepared from the alkoxide solution via the dip-coating technique affecting the photocatalytic decomposition of aqueous acetic acid. *J. Mater. Sci.* **1994**, *29*, 5911–5915, https://doi.org/10.1007/bf00366875.
214. Puma, G.L.; Bono, A.; Krishnaiah, D.; Collin, J.G. Preparation of titanium dioxide photocatalyst loaded onto activated carbon support using chemical vapor deposition: A review paper. *J. Hazard. Mater.* **2008**, *157*, 209–219, https://doi.org/10.1016/j.jhazmat.2008.01.040.
215. Zhang, Y.; Li, Q.Synthesis and characterization of Fe-doped TiO_2 films by electrophoretic method and its photocatalytic ac-tivity toward methyl orange. *Solid State Sci.* **2013**, *16*, 16–20.
216. Damodar, R.A.; Swaminathan, T. Performance evaluation of a continuous flow immobilized rotating tube photocatalytic reactor (IRTPR) immobilized with TiO_2 catalyst for azo dye degradation. *Chem. Eng. J.* **2008**, *144*, 59–66.
217. Huang, Y.; Wang, P.; Wang, Z.; Rao, Y.; Cao, J.; Pu, S.; Ho, W.; Lee, S.C. Protonated g-C_3N_4/Ti^{3+} self-doped TiO_2 nanocompo-site films: Room-temperature preparation, hydrophilicity, and application for photocatalytic NOx removal. *Appl. Catal. B Environ.* **2019**, *240*, 122–131.
218. Wang, M.; Zhang, L.; Huang, W.; Xiu, T.; Zhuang, C.; Shi, J. The catalytic oxidation removal of low-concentration HCHO at high space velocity by partially crystallized mesoporous MnO_x. *Chem. Eng. J.* **2017**, *320*, 667–676.
219. Zhou, L.; He, J.; Zhang, J.; He, Z.; Hu, Y.; Zhang, C.; He, H. Facile In-Situ Synthesis of Manganese Dioxide Nanosheets on Cellulose Fibers and their Application in Oxidative Decomposition of Formaldehyde. *J. Phys. Chem. C* **2011**, *115*, 16873–16878, https://doi.org/10.1021/jp2050564.
220. Miyawaki, J.; Lee, G.-H.; Yeh, J.; Shiratori, N.; Shimohara, T.; Mochida, I.; Yoon, S.-H. Development of carbon-supported hybrid catalyst for clean removal of formaldehyde indoors. *Catal. Today* **2012**, *185*, 278–283, https://doi.org/10.1016/j.cattod.2011.09.036.

221. Li, J.; Zhang, P.; Wang, J.; Wang, M. Birnessite-Type Manganese Oxide on Granular Activated Carbon for Formaldehyde Removal at Room Temperature. *J. Phys. Chem. C* **2016**, *120*, 24121–24129, https://doi.org/10.1021/acs.jpcc.6b07217.
222. Liu, Q.; Ke, M.; Liu, F.; Yu, P.; Hu, H.; Li, C. High-performance removal of methyl mercaptan by nitrogen-rich coconut shell activated carbon. *RSC Adv.* **2017**, *7*, 22892–22899, https://doi.org/10.1039/c7ra03227g.
223. Sikkema, J.K.; Ong, S.K.; Alleman, J.E. Photocatalytic concrete pavements: Laboratory investigation of NO oxidation rate under varied environmental conditions. *Constr. Build. Mater.* **2015**, *100*, 305–314.
224. Todorova, N.; Giannakopoulou, T.; Karapati, S.; Petridis, D.; Vaimakis, T.; Trapalis, C. Composite TiO_2/clays materials for photocatalytic NOx oxidation. *Appl. Surf. Sci.* **2014**, *319*, 113–120.
225. Folli, A.; Pade, C.; Hansen, T.B.; De Marco, T.; Macphee, D.E. TiO_2 photocatalysis in cementitious systems: Insights into self-cleaning and depollution chemistry. *Cem. Concr. Res.* **2012**, *42*, 539–548, https://doi.org/10.1016/j.cemconres.2011.12.001.
226. Bianchi, C.L.; Pirola, C.; Galli, F.; Vitali, S.; Minguzzi, A.; Stucchi, M.; Manenti, F.; Capucci, V. NOx degradation in a continuous large-scale reactor using full-size industrial photocatalytic tiles. *Catal. Sci. Technol.* **2016**, *6*, 2261–2267.
227. Maggos, T.; Bartzis, J.; Liakou, M.; Gobin, C. Photocatalytic degradation of NOx gases using TiO_2-containing paint: A real scale study. *J. Hazard. Mater.* **2007**, *146*, 668–673, https://doi.org/10.1016/j.jhazmat.2007.04.079.
228. Gallus, M.; Ciuraru, R.; Mothes, F.; Akylas, V.; Barmpas, F.; Beeldens, A.; Bernard, F.; Boonen, E.; Boréave, A.; Cazaunau, M.; et al. Photocatalytic abatement results from a model street canyon. *Environ. Sci. Pollut. Res.* **2015**, *22*, 18185–18196, https://doi.org/10.1007/s11356-015-4926-4.
229. Gallus, M.; Akylas, V.; Barmpas, F.; Beeldens, A.; Boonen, E.; Boreave, A.; Cazaunau, M.; Chen, H.; Daele, V.; Doussin, J.F.; et al. Photocatalytic de-pollution in the Leopold II tunnel in Brus-sels: NOx abatement results. *Build. Environ.* **2015**, *84*, 125–133.
230. Ballari, M.; Brouwers, H. Full scale demonstration of air-purifying pavement. *J. Hazard. Mater.* **2013**, *254–255*, 406–414, https://doi.org/10.1016/j.jhazmat.2013.02.012.
231. Folli, A.; Strøm, M.; Madsen, T.P.; Henriksen, T.; Lang, J.; Emenius, J.; Klevebrant, T.; Nilsson, A. Field study of air purifying paving elements containing TiO_2. *Atmos. Environ.* **2015**, *107*, 44–51, https://doi.org/10.1016/j.atmosenv.2015.02.025.
232. Huang, Y.; Zhang, J.; Wang, Z.; Liu, Y.; Wang, P.; Cao, J.J.; Ho, W.K. g-C_3N_4/TiO_2 composite film in the fabrication of a photocatalytic air-purifying pavements. *Sol. RRL* **2020**, *4*, 2000170.
233. Lorencik, S.; Yu, Q.L.; Brouwers, H.J.H. Design and performance evaluation of the functional coating for air purification under indoor conditions. *Appl. Catal. B Environ.* **2015**, *168*, 77–86.
234. Gandolfo, A.; Bartolomei, V.; Alvarez, E.G.; Tlili, S.; Gligorovski, S.; Kleffmann, J.; Wortham, H. The effectiveness of indoor photocatalytic paints on NO_x and HONO levels. *Appl. Catal. B Environ.* **2015**, *166-167*, 84–90, https://doi.org/10.1016/j.apcatb.2014.11.011.
235. Boonen, E.; Akylas, V.; Barmpas, F.; Bottalico, L.; Boreave, A.; Cazaunau, M.; Chen, H.; Daele, V.; de Marco, T.; Doussin, J.F.; et al. Construction of a photocatalytic de-polluting field site in the Leopold II tunnel in Brussels. *J. Environ. Manag.* **2015**, *155*, 136–144.
236. Guerrini, G.L. Photocatalytic performances in a city tunnel in Rome: NO_x monitoring results. *Constr. Build. Mater.* **2012**, *27*, 165–175, https://doi.org/10.1016/j.conbuildmat.2011.07.065.
237. Maggos, T.; Plassais, A.; Bartzis, J.G.; Vasilakos, C.; Moussiopoulos, N.; Bonafous, L. Photocatalytic degradation of NO_x in a pilot street canyon configuration using TiO_2-mortar panels. *Environ. Monit. Assess.* **2007**, *136*, 35–44, https://doi.org/10.1007/s10661-007-9722-2.
238. Ao, C.; Lee, S.-C. Indoor air purification by photocatalyst TiO_2 immobilized on an activated carbon filter installed in an air cleaner. *Chem. Eng. Sci.* **2005**, *60*, 103–109, https://doi.org/10.1016/j.ces.2004.01.073.
239. Denny, F.; Permana, E.; Scott, J.; Wang, J.; Pui, D.Y.H.; Amal, R. Integrated Photocatalytic Filtration Array for Indoor Air Quality Control. *Environ. Sci. Technol.* **2010**, *44*, 5558–5563, https://doi.org/10.1021/es100421u.
240. Jo, W.-K.; Tayade, R.J. New Generation Energy-Efficient Light Source for Photocatalysis: LEDs for Environmental Applications. *Ind. Eng. Chem. Res.* **2014**, *53*, 2073–2084, https://doi.org/10.1021/ie404176g.
241. Slimen, H.; Ochiai, T.; Nakata, K.; Murakami, T.; Houas, A.; Morito, Y.; Fujishima, A. Photocatalytic Decomposition of Cigarette Smoke Using a TiO_2-Impregnated Titanium Mesh Filter. *Ind. Eng. Chem. Res.* **2011**, *51*, 587–590, https://doi.org/10.1021/ie2016762.
242. Negishi, N.; Sano, T. Photocatalytic Solar Tower Reactor for the Elimination of a Low Concentration of VOCs. *Molecules* **2014**, *19*, 16624–16639, https://doi.org/10.3390/molecules191016624.
243. Cyranoski, D. China tests giant air cleaner to combat urban smog. *Nature* **2018**, *555*, 152–153.
244. Cao, J. The Importance of Aerosols in the Earth System: Science and Engineering Perspectives. *Aerosol Sci. Eng.* **2017**, *1*, 1–6, https://doi.org/10.1007/s41810-017-0005-1.
245. Cao, Q.; Kuehn, T.H.; Shen, L.; Chen, S.-C.; Zhang, N.; Huang, Y.; Cao, J.; Pui, D.Y. Urban-scale SALSCS, Part I: Experimental Evaluation and Numerical Modeling of a Demonstration Unit. *Aerosol Air Qual. Res.* **2018**, *18*, 2865–2878, https://doi.org/10.4209/aaqr.2018.06.0238.
246. Cao, Q.; Huang, M.; Kuehn, T.H.; Shen, L.; Tao, W.-Q.; Cao, J.; Pui, D.Y. Urban-scale SALSCS, Part II: A Parametric Study of System Performance. *Aerosol Air Qual. Res.* **2018**, *18*, 2879–2894, https://doi.org/10.4209/aaqr.2018.06.0239.
247. Das, R.; Vecitis, C.D.; Schulze, A.; Cao, B.; Ismail, A.F.; Lu, X.; Chen, J.; Ramakrishna, S. Recent advances in nanomaterials for water protection and monitoring. *Chem. Soc. Rev.* **2017**, *46*, 6946–7020, https://doi.org/10.1039/c6cs00921b.

248. Abidi, M.; Assadi, A.; Bouzaza, A.; Hajjaji, A.; Bessais, B.; Rtimi, S. Photocatalytic indoor/outdoor air treatment and bacterial inactivation on CuxO/TiO_2 prepared by HiPIMS on polyester cloth under low intensity visible light. *Appl. Catal. B Environ.* **2019**, *259*, 118074, https://doi.org/10.1016/j.apcatb.2019.118074.
249. Castillo, M.V.; Lucerob, J.O.S.; Arriagaa, S. Photocatalytic inactivation of airborne microorganisms in continuous flow using perlite-supported ZnO and TiO_2. *Chem. Eng. J.* **2019**, *374*, 914–923.
250. Chen, Y.; Liao, C.; Shen, W.; Su, C.; Wu, Y.; Tsai, M.; Hsiao, S.; Yu, K.; Tseng, C. Effective disinfection of airborne microbial contamination in hospital wards using a zero-valent nano-silver/TiO_2-chitosan composite. *Indoor Air* **2019**, *29*, 439–449.
251. Mamba, G.; Gangashe, G.; Moss, L.; Hariganesh, S.; Thakur, S.; Vadivel, S.; Mishra, A.K.; Vilakati, G.D.; Muthuraj, V.; Nkambule, T.T.I. State of the art on the photocatalytic applications of graphene based nanostructures: From elimination of hazardous pollutants to disinfection and fuel generation. *J. Environ. Chem. Eng.* **2020**, *8*, 103505.